
This is an electronic reprint of the original article.
This reprint may differ from the original in pagination and typographic detail.

Taimuri, Ghalib; Kim, Sang Jin; Mikkola, Tommi; Hirdaris, Spyros

A two-way coupled FSI model for the rapid evaluation of accidental loads following ship hard grounding

Published in:
Journal of Fluids and Structures

DOI:
[10.1016/j.jfluidstructs.2022.103589](https://doi.org/10.1016/j.jfluidstructs.2022.103589)

Published: 01/07/2022

Document Version
Publisher's PDF, also known as Version of record

Published under the following license:
CC BY

Please cite the original version:
Taimuri, G., Kim, S. J., Mikkola, T., & Hirdaris, S. (2022). A two-way coupled FSI model for the rapid evaluation of accidental loads following ship hard grounding. *Journal of Fluids and Structures*, 112, Article 103589. <https://doi.org/10.1016/j.jfluidstructs.2022.103589>

This material is protected by copyright and other intellectual property rights, and duplication or sale of all or part of any of the repository collections is not permitted, except that material may be duplicated by you for your research use or educational purposes in electronic or print form. You must obtain permission for any other use. Electronic or print copies may not be offered, whether for sale or otherwise to anyone who is not an authorised user.



Contents lists available at ScienceDirect

Journal of Fluids and Structures

journal homepage: www.elsevier.com/locate/jfs

A two-way coupled FSI model for the rapid evaluation of accidental loads following ship hard grounding

Ghalib Taimuri^a, Sang Jin Kim^{a,b}, Tommi Mikkola^a, Spyros Hirdaris^{a,*}

^a Aalto University, Maritime Technology Group, Espoo, Finland

^b National Sun Yat-sen University, Department of Marine Env. & Eng., Taiwan



ARTICLE INFO

Article history:

Received 27 July 2021

Received in revised form 17 March 2022

Accepted 26 April 2022

Available online xxx

Keywords:

Fluid–structure interactions

Accidental loads

Contact mechanics

Ship grounding dynamics

ABSTRACT

The assessment of structural crashworthiness following ship grounding events should consider the influence of multi-physics on dynamic response. To date, this has been achieved by computationally expensive approaches combining explicit 3D FEA with hydrodynamic solvers (e.g. Conti et al. (2021); Kim et al. (2021)). To offer an alternative, this paper presents a rapid six degree of freedom (6-DoF) two-way coupled fluid–structure interaction (FSI) model that could be used for the rapid evaluation of ship dynamic response and structural crashworthiness during hard grounding events. The time domain solution is based on a simplified contact analysis model that combines the external dynamics idealization of Taimuri et al. (2020) with an extended version of the internal mechanics analytical formulation of Simonsen (1997a) and Sun et al. (2017). The plate cutting angle is calibrated based on the rock geometry and hull indentation. A ray-tracing algorithm that utilizes panels and the tip of a conical rock is implemented to idealize hull penetration. The model is numerically validated by comparing results against LS-DYNA simulations for a box-shaped barge of double bottom configuration and a passenger vessel. Parametric studies demonstrate that longitudinal and vertical forces produced by different models compare well. However, the lateral forces for the study case of a passenger ship progressing along a straight path are shown to be underestimated. This is because the proposed method (i) does not allow for the influence of lateral loading on longitudinal hull members and (ii) overestimates the forces in regions of extreme curvature (e.g. fore shoulder, bow and boundaries of the hull).

© 2022 The Author(s). Published by Elsevier Ltd. This is an open access article under the CC BY license (<http://creativecommons.org/licenses/by/4.0/>).

1. Introduction

Ship collisions and groundings are of great significance as ship accidents persist regardless of regulatory progress. Allianz Global (2020) reports that ship groundings have been the second biggest cause of ship losses during the past decade. Factors contributing to ship grounding accidents relate to machinery failures, human factors, traffic complexity and environmental conditions. Consequences may be foundering leading to sinking or submerging of marine vessels, environmental pollution, traffic flow interruption and loss of human life.

Grounding events arise when ships crash into the seabed or run onto protruding rocks. Hence, ship grounding dynamics are complex and interlink with maneuvering forces, environmental loads emerging from short waves, wind, ocean currents and an increase of ship resistance. The dynamics of ship grounding can be studied by model tests or fully coupled fluid–structure interaction (FSI) methods. The former are very expensive, time consuming and may lead to results that are

* Corresponding author.

E-mail address: spyros.hirdaris@aalto.fi (S. Hirdaris).

Nomenclature

3D	Three dimensional
AGCS	Allianz Global Corporate and Specialty
ALE	Arbitrary Lagrangian–Eulerian
CFD	Computational Fluid Dynamics
CoG	Center of Gravity
DoF	Degrees of Freedom
FEA	Finite Element Analysis
FSB	Floodstand Ship B
FSI	Fluid–Structure Interaction(s)
HELCOM	Helsinki-Commission
LS-DYNA	Livermore Software Dynamic solver
MCOL	Mitsubishi Collision
NSWC	Naval Surface Warfare Center
A_{wp}	Waterplane area (m ²)
B	Beam of the ship (m)
B_{de}	Deformation width (m)
\mathbf{B}_p	Radiation damping matrix
\mathbf{B}_H	Hydrodynamic damping matrix
$b_{l,Gir}$	Spacing between two longitudinal girders (m)
$b_L, b_{l,Stiff}$	Spacing between longitudinal stiffeners (m)
\mathbf{C}	Rigid body Coriolis and centripetal forces matrix
C_B	Ship block coefficient
D_{DB}	Spacing between the inner and outer bottom (m)
D_t	Height of transverse frame (m)
D_w	Height of longitudinal stiffener (height of web) (m)
d_f	Stiffener flange width (m)
E	Young's Modulus (Pa)
$\dot{E}_c, \dot{E}_f, \dot{E}_p$	crack, friction and plastic Energy dissipation rate (Nm/s)
F_{Bulk_i}	Intact bulkhead plastic resistance force (N)
F_{Bulk_f}	Fractured bulkhead plastic resistance force (N)
\mathbf{F}_C	Contact force (N) and moment (Nm) vector.
$F_{FXc,global}$	Frictional contact force in a global coordinate system (N)
$F_{FYc,global}$	
$F_{FZc,global}$	
F_{grx}	Total contact force in body-fixed coordinate system (N)
F_{gry}	
F_{grz}	
F_H	Horizontal resistance and reaction force of structure (N)
F_{floor}	Plastic floor resistance (N)
F_{Gir}	Plastic girder resistance (N)
F_n	Froude number
F_P	Plastic resistance force of structure (N)
F_{plate_i}	Intact plate plastic resistance force (N)
F_{plate_f}	Fractured plate plastic resistance force (N)
\mathbf{F}_{prop}	Propeller force (N)
$F_{PXc,global}$	Plastic contact force in a global coordinate system (N)
$F_{PYc,global}$	
$F_{PZc,global}$	
\mathbf{F}_{Rud}	Rudder force vector (N) and (Nm)
F_{Stif_i}	Intact stiffener plastic resistance force (N)
F_{Stif_f}	Fractured stiffener plastic resistance force (N)

\mathbf{F}_{sw}	Shortwaves force vector (N) and (Nm)
$F_{TXc,global}$	
$F_{TYc,global}$	Total contact force in a global coordinate system (N)
$F_{TZc,global}$	
F_V	Vertical resistance and reaction force of structure (N)
G_x, G_y, G_z	Total number of block in x, y, and z direction for storing panel ids
GM_{T0}, GM_{L0}	Transverse and longitudinal initial metacentric height.
g	Acceleration of gravity (9.807 m/s ²); horizontal to plastic force ratio
H_{def}	Height of the transverse floor deformation (m)
I_x, I_y, I_z	Roll, pitch, and yaw moment of inertia (kg m ²)
\mathbf{K}	Restoring force matrix
K_G	Vessels' CoG measured from keel (m)
$K_{\dot{p}}$	Variation of roll moment due to roll acceleration (kg.m ²)
$K_{\dot{r}}$	Variation of roll moment due to yaw acceleration (kg.m ²)
$K_{\dot{v}}$	Variation of roll moment due to sway acceleration (kg.m)
k	vertical to horizontal force ratio
loc_{floor}	Location of the transverse floor from base of the rock (m)
L_{pp}	Length between perpendiculars (m)
\mathbf{M}	Inertia matrix
\mathbf{M}_A	Added inertia matrix
M_0	Plastic bending moment of plate per unit length (Nm)
$M_{\dot{q}}$	Variation in pitch moment due to pitch acceleration (kg.m ²)
m	Mass of the ship (kg)
mod	computes the remainder of the division
N_0	Plastic membrane force of plate per unit length (N)
$N_{\dot{v}}$	Variation in yaw moment due to sway acceleration (kg.m)
$N_{\dot{r}}$	Variation in yaw moment due to yaw acceleration (kg.m ²)
ϵ_{cr}	Material strain hardening
N'_v, N'_r	Effect of sway and yaw linear velocities on yawing moment
N'_{vvv}, N'_{rrr}	Changes in yaw moment due to higher-order pure sway velocity and yaw velocity
N'_{vvr}, N'_{rvr}	Coupled effect of sway and yaw velocity on yaw moment
p, q, r	Angular (roll, pitch & yaw) velocities in the body-fixed coordinate system (m/s)
$p_{CoG}, q_{CoG}, r_{CoG}$	Angular (roll, pitch & yaw) velocities at CoG (m/s)
$\dot{p}, \dot{q}, \dot{r}$	Angular (roll, pitch & yaw) acceleration in the body-fixed coordinate system (rad/s ²)
\vec{R}	Translational Earth-fixed position vector
\vec{R}_{Gr}	Rock position vector in earth fixed coordinate system [X_{Gr}, Y_{Gr}, Z_{Gr}]
R_c	Ductile fracture toughness of material (Pa.m)
R_n, R_{n+1}	Consecutive peaks of undamped response
R_R	Rounded tip radius of rock (m)
r_0	Ship body fixed origin
\vec{r}_G	Position vector from r_0 to CoG [x_G, y_G, z_G]
$s_{l,c}$	Critical transverse location of longitudinal stiffener from rock tip (m)
$s_{l,f}$	Distance to the deformed stiffener from rock tip (m)
T	Ship draft (m)
\mathbf{T}_R	Transformation matrix of angular velocities
\mathbf{T}_T	Transformation matrix of translational velocities
t	Plate thickness (m)
t_f	Stiffener flange thickness (m)
t_l	Thickness of longitudinal bulkheads and girders (m)
t_t	Transverse floor thickness (m)
t_w	Stiffener web thickness (m)
U	Instantaneous ship speed and relative velocity between the ship and a rock (m/s)

u, v, w	Translational (surge, sway & heave) velocities in body-fixed coordinate system (m/s)
$u_{CoG}, v_{CoG}, w_{CoG}$	Translational (surge, sway & heave) velocities at CoG (m/s)
u_{global}	Hull panel intersection velocities in global (inertial) coordinate system (m/s)
v_{global}	
w_{global}	
$u_{int}, v_{int}, w_{int}$	Hull panel velocity at intersection point (m/s)
$\dot{u}, \dot{v}, \dot{w}$	Translational (surge, sway & heave) acceleration in body-fixed coordinate system (rad/s ²)
u_0, v_0	Plate longitudinal and transversal gap openings (m)
$X_{\dot{u}}$	Variation in longitudinal force due to surge acceleration (kg)
$X'_{vr}, X'_{vv}, X'_{rr}, X'_{vvv}$	X-directional resistance addition due to ship motions in pure sway, pure yaw and coupled influence of sway and yaw velocities in the longitudinal direction
x_f	Location of center of flotation measured from CoG (m), +ve bow
x_G	Longitudinal distance of the center of gravity measured from midship (m), +ve bow (m)
$x_{int}, y_{int}, z_{int}$	Location of rock tip from ship origin (m)
Y_{Hull}	External sway damping forces (N)
$Y_{\dot{p}}$	Variation in lateral force due to roll acceleration (kg·m)
$Y_{\dot{r}}$	Variation in lateral force due to yaw acceleration (kg·m)
$Y_{\dot{v}}$	Variation in lateral force due to sway acceleration (kg)
Y'_{vr}, Y'_{rr}	Effect of sway and yaw linear velocities on lateral force
Y'_{vvr}, Y'_{vvr}	Coupled effect of sway and yaw velocity on sway force and yaw moment
Y'_{vvv}, Y'_{rrr}	Changes in lateral force (Y') and yaw moment (N') due to higher-order pure sway velocity and yaw velocity.
$Z_{\dot{q}}$	Variation in heave force due to pitch acceleration (kg·m)
$Z_{\dot{w}}$	Variation in heave force due to heave acceleration (kg)
z_G	Vertical distance of the center of gravity measured from midship and still waterline +ve towards keel (m)
$0 - X, Y, Z$	Earth fixed coordinate system (m)
$0 - X_{Gr}, Y_{Gr}, Z_{Gr}$	Rock position in Earth fixed coordinate system (m)
$0 - x, y, z$	body-fixed coordinate system (m)
α	Plate flap angle (rad); transverse floor bending angle (rad)
$\Delta_x, \Delta_y, \Delta_z$	Size of a 3D sub-block
δ_{fra}	Plate fracture penetration (m)
δ_{out}	Penetration into the hull (m)
$\epsilon_f = \epsilon_{floor}$	Transverse floor critical strain of fracture
ξ	Plate curls rolling angle (rad)
$\zeta_w, \zeta_\phi, \zeta_\theta$	Heave, roll and pitch damping ratios
$\theta, \theta_p, \theta_{p,imm}$	Plate split angle (rad)
θ_t	Transverse floor deformation angle (rad)
ϕ, ϕ_c	Cone semi-apex angle and critical cone apex angle (rad)
Δ_t	Deflection of transverse floor (m)
ρ	Water density (kg/m ³)
ϕ, θ, ψ	Roll, pitch and yaw rotation (rad)
ψ_C	Plate wrapping angle on rounded rock tip (rad)
ω	Angular velocity vector (rad/s)
$\omega_w, \omega_\phi, \omega_\theta$	Heave, roll and pitch angular frequencies
γ	Euler angle
μ	Coefficient of friction
σ_y	Yield strength of material (Pa)
σ_0	Flow stress of material (Pa)
χ_t	Longitudinal spacing of transverse member

difficult to explain at full scale (e.g. see [Kitamura and Kuriowa, 1996](#); [Lemmen et al., 1996](#); [Rodd, 1996a,b](#); [Rodd and Sikora, 1995](#)). In theory emerging multiphysics methods can provide a useful alternative (e.g. [Rudan et al., 2019](#); [Song et al., 2016](#);

Kim et al., 2021). However, with the exception of the Super Element method they are computationally uneconomic (Kim et al., 2022b). The latter is important, especially considering that the mitigation of grounding risks requires accurate and fast estimation of hull damage extents and the development of Risk Control Options for use in ship design for safety (Conti et al., 2021; Zhang et al., 2021).

To offer a scientifically sound yet practical alternative this paper introduces a rapid time-domain two-way coupled FSI model. The method combines 6-DoF ship maneuvering motions with a model accounting for structural deformations and the influence of hydrodynamic properties in way of grounding contact. The assessment of structural deformation is based on the energy dissipation approaches of Simonsen (1997a) and Sun et al. (2017). The multiphysics crashworthiness model presented advances the state of the art by allowing for:

- The influence of plate split angle variations at different penetration depths. Consequently, the splitting angle of the plate is defined as a function of rock penetration and base-radii. Likewise, the extent of plate deformations depends on out-of-plane ship motions.
- The variation of the inner and outer bottom plate split angles that were considered equivalent in past models.
- The evaluation of dynamic rock–ship interactions, through a rapid coupling algorithm that combines internal and external mechanics at the interface of the rock tip with the ship's bottom.

Results validated for the case of a passenger vessel subject to hard grounding with a conical rock suggest that the method is computationally robust, economic while it accounts for environmental loads (wind, shortwaves, and ocean currents). Thus it could be used for low-fidelity ship design and optimization, to introduce new damage extend datasets, rules and regulations for ship damage stability assessment and for the development of intelligent decision support systems for use in emergency response.

The paper is organized in five sections as follows. State of the art research in ship grounding is reviewed in Section 2. The fundamentals of the novel FSI method and associated assumptions are explained in Section 3. The validation of the rapid FSI model against LS-DYNA simulations and discussion of the results are included in Section 4. Conclusions are drawn in Section 5.

2. Literature survey

A review of several applications implementing FSI methods for the evaluation of loads and responses is given by Hirdaris et al. (2014) and Hirdaris and Mikkola (2021). The evaluation of sea loads associated with accidental events such as ship collisions (e.g. Choung et al., 2020; Lee et al., 2017; Rudan et al., 2019; Song et al., 2017; Zhang and Suzuki, 2006), groundings (e.g. Kim et al., 2022b, 2021, 2020; Lee et al., 2017) and ship–ice interactions (Lu and Zou, 2020; Luo et al., 2020; Song et al., 2016; Wang and Derradji-Aouat, 2010) account for the influence of contact mechanics by novel FSI models. The use of such multiphysics methods for the assessment of ship loads in intact or damaged conditions requires considerable computational time because of two-way coupling and the fidelity of FEA models (Kim et al., 2021; Lakshmyanarayanan and Hirdaris, 2020). This is the reason why the derivation of simplified modeling approaches (e.g. empirical methods, super element methods, and contact mechanics models) remains relevant within the context of developing advanced regulations for ship design assessment and the risk management of shipping operations (e.g. Idrissova et al., 2019; Descantes et al., 2019; Conti et al., 2021; Zhang et al., 2021).

Modeling grounding dynamics consists of two processes namely external dynamics and internal mechanics. A summary of published work on the subject is given in Table 1. Accounting for the influence of hydrodynamics in way of contact (e.g., added mass and damping effects due to ship motions, evasive actions following a maneuvering path) relates to external dynamics. Internal mechanics mostly encompass structural responses and deformation because of energy dissipation post-mortem a grounding event. The influence of evasiveness has been traditionally ignored in these models. The latter may be considered disadvantageous especially considering that as a ship maneuvers in shallow waters a wide range of seabed topologies namely rocks, shoals, and reefs may be evident (Alsos and Amdahl, 2007). In literature, rocks encountered in hard grounding scenarios are idealized as pinnacles or truncated cones that will rupture the hull bottom. Shoals have large and soft contact area (Ehlers, 2011) where typically a hull girder may collapse and the bottom structure may experience crushing and denting. Reefs can be idealized as conical rocks (Simonsen, 1997b). A ship's striking on a rock, or a shoal is termed power grounding (bottom raking and bottom sliding). In some occasions, stranding may be followed by grounding (Rizzuto et al., 2018; Souliotis and Samuelides, 2013).

As part of modeling internal mechanics a ship's structural deformation can be predicted by empirical methods (Minorsky, 1958), FEA (Kim et al., 2020; Liu et al., 2021), the super element method (Buldgen et al., 2012; Kim et al., 2022b; Le Sourné et al., 2012), experimental approaches (e.g. Calle et al., 2020; Rodd, 1996a,b; Rodd and Sikora, 1995) or simplified analytical models (Zhang et al., 2019). External dynamics have been modeled by the so-called decoupled methods that traditionally tend to ignore the influence of fluid dynamics and predict the energy due to impact by analytical expressions or FEA (e.g. Liu et al., 2017; Yu et al., 2019; Ehlers, 2011; Pill and Tabri, 2011). Decoupled FEA simulations have been used for ship structural design optimization (e.g. Song and Hu, 2017; Zeng et al., 2016), to idealize plastic deformation (Abubakar and Dow, 2013) and to introduce empirical formulae emerging from force penetration curves (Heinvee and Tabri, 2015). Recently, Kim et al. (2020, 2021) presented large scale numerical crashworthiness analysis methods that account for the

Table 1
Summary of methods for ship grounding simulation^a.

Article	Internal mechanics	External dynamics		DoF	Ship Type	Grounding		Obstacle	Results evaluated	Model size
	Method	Decoupled	Coupled			Type	Case			
Simonsen (1997a)	Theoretical		Quasi-static equilibrium	Surge, Heave, Roll, Pitch	Tanker	HG, SG	Raking	Rock	Damage Length, Dissipation Energy, Resistance Force, Penetration	Par.Sec (NSWC)
Matusiak (2002)	Point Force		Hybrid method	6-DoF	Ro-Ro	HG	Raking	Point	Resistance Force, Ship Motions	Panel
Hong and Amdahl (2012)	Theoretical	Dry		Surge	Tanker	HG	Raking	Shoal	Dissipation Energy, Resistance Force, Penetration	Par.Sec(DB)
Nguyen et al. (2011)	Analytical Equation & FEM(LS)		Hybrid method	Surge, Heave, Pitch	Tanker	HG	Raking	Shoal	Damage Length, Resistance Force, Penetration	Par.Sec(DB)
Abubakar and Dow (2013)	FEM (AB)	Dry		Surge	Tanker	HG	Raking	Cone	Dissipation Energy, Resistance Force, Damage Length, Penetration	Par.Sec (NSWC1)
Heinvee and Tabri (2015)	FEM (LS)	Dry		Surge	Tanker	HG	Raking	rock	Resistance Force, Ship Motions	Par.Sec(DB)
Zeng et al. (2016)	Theory & FEM (LS)	Dry		Surge	Tanker	HG	Raking	Rock	Resistance Force	Par.Sec(DB)
Yu et al. (2016), Yu and Amdahl (2016)	FEM (LS)		Hybrid method	6-DoF	Supply Vessel	SG	Raking	Rigid plate	Dissipation Energy, Resistance Force, Ship Motions	Par.Sec(Fore)
Sun et al. (2017)	Theoretical & FEM (LS)	Dry		Surge	Tanker	HG	Raking	Rock	Resistance Force,	Par.Sec(DB)
Lee et al. (2017, 2013)	ALE & FEM (LS)		Strongly coupled, FSI	6-DoF	Specialized Ship	HG	Raking	Rock	Dissipation Energy, Resistance Force	Full FEM model of ship
Song and Hu (2017)	Theoretical	Dry		Surge	Tanker	HG	Raking	Rock, shoal	Dissipation Energy, Resistance Force	Par.Sec(DB)
Prabowo et al. (2017)	FEM (LS)	Dry		Surge	Tanker	HG	Raking	Rock	Damage Length, Dissipation Energy, Resistance Force	Par.Sec(DB)
Calle et al. (2017)	Exp and FEM (LS)	Dry		Surge	Tanker	HG	Raking, Stranding	Wedge	Resistance Force, Ship Motions, Penetration	Par.Sec(DB)
Prabowo et al. (2020)	FEM (LS)	Dry		Surge	Tanker	HG	Raking, Stranding	Cone, shoal	Dissipation Energy, Resistance Force	Par.Sec(DB)
Liu et al. (2021)	FEM (LS)	Dry		Surge	Container Ship	HG	Raking, Stranding	Cone	Dissipation Energy, Resistance Force	Par.Sec(DB)
Chen and Guedes Soares (2020)	Exp and FEM (LS)	Dry		Heave	Tanker	HG	Stranding	Cylindrical Indenter	Resistance Force	Web.G + Stiff
Brubak et al. (2021)	FEM (LS & AB)	Dry		Surge	Tanker	HG	Raking	Rock	Dissipation Energy, Resistance Force	Par.Sec, NSWC

(continued on next page)

Table 1 (continued).

Article	Internal mechanics	External dynamics			Ship Type	Grounding		Obstacle	Results evaluated	Model size
	Method	Decoupled	Coupled	DoF		Type	Case			
Kim et al. (2021, 2020)	CFD (resistance) FEM (LS)		Unified, FSI Model	6-DoF	Cruise Ship	HG	Raking	Shoal, Rock	Damage Length, Dissipation Energy, Resistance Force, Penetration, Ship motions	Full FEM model of the ship
Kim et al. (2022a)	FEM (LS)		Hybrid method	6-DoF	Cruise & Barge	HG	Raking	Shoal, Rock	Damage Length, Dissipation Energy, Ship motions	Full FEM model of the ship
Kim et al. (2022b)	Super element Method		Hybrid method	6-DoF	Cruise Ship	HG	Raking	Rock	Damage Length, Dissipation Energy, Penetration	Bottom structure
Current paper	Theoretical		Maneuvering FSI	6-DoF	Cruise & Barge	HG	Raking	Rock	Damage Length, Dissipation Energy, Resistance Force, Penetration, Ship motions	Panel + Comp.Str of DB

^aNote: FEM: Finite Element Method, Exp: Model Scale Experiments, Theoretical: Theoretical upper bound plastic deformation method, CFD: Computational Fluid Dynamics, LS: LS-DYNA, AB: Abaqus, ALE: Arbitrary Lagrangian–Eulerian; FSI: Fluid-Structure interaction; DoF: Degrees of Freedom, Ro-Ro: Roll on Roll off Ship; Par.Sec: Partial section of Ship, DB: Double bottom structure, Fore: Fore ship section, Web.G: Web girder, Stiff: Stiffeners, Comp.Str: Complete structural detail, NSWC: Naval Surface Warfare Center Model (Rodd, 1996a,b), Pan: Panel model of full ship without structure details; HG: hard grounding; SG: Soft Grounding.; Dry: without external mechanics.

effects of ship grounding dynamics. This work demonstrates that the influence of hydrodynamic restoring forces may also be significant and if coupling effects are ignored the ship may ascend erratically after her initial contact with the seabed.

The computational expense of the above mentioned large scale multiphysics methods, implies the need to develop simplified approaches for use in rapid design development and assessment. Lately such reduced order integration methods have been presented by Kim et al. (2022a,b). The former makes use of the so-called Super-Element method of Le Sourne et al. (2012) according to which a structure is divided into several macro elements (e.g., plates, intersections, transverse and longitudinal members) and forces associated with the structural resistance of each of those is described by closed-form analytical expressions. As elements deform individually, the aggregate of their deformation is used to express the total structural deformation of the ship in accidental conditions. The paper by Kim et al. (2022a) demonstrates an alternative approach that combines simplified spring elements for the idealization of restoring forces and an FEA model for the idealization of grounding dynamics.

A critical review of the above leads to the conclusion that relatively few studies demonstrate the influence of direct coupling of mechanics while accounting for hydrodynamic actions. An exception to the rule are the recent models presented by Kim et al. (2022a,b) and Lee et al. (2017, 2013). The papers by Lee et al. (2017, 2013) and Kim et al. (2021) demonstrate that strongly coupled ship grounding dynamics can be idealized by advanced discretization solvers such as Arbitrary Lagrangian–Eulerian (ALE) and nonlinear FEM possibly with spring element corrections to account for the influence of restoring forces. Yet computational economy is an issue with such type of large-scale models. On the other hand, the work by Kim et al. (2022b) confirms the emergence of the Super Element method as a possible alternative. However, even this approach should be validated further and maybe inevitably inaccurate in terms of modeling complex geometries, rock dynamics and ship dynamics.

3. FSI method

In this work, the 6-DoF dynamics of a rigid ship are coupled with an analytical contact mechanics model. Coupling is implemented by a contact detection algorithm. An enhanced technique is proposed to determine the instantaneous change of plate splitting angle. The model has been validated by LS-DYNA FEA simulations encompassing a hydrodynamic model that accounts for the influence of hydrodynamic inertia, damping, memory effects and restoring forces and moments via the ‘Mitsubishi Collision – MCOL’ (Ferry et al., 2002; Le Sourne, 2007) algorithm.

Fig. 1 illustrates the process of solving a simplified two-way coupled partitioned approach that transfers information from external to internal mechanics at each time step. Ship maneuvering data, structural information and rock parameters are accounted for by the method. At the initialization stage, the shape of the hull is used to form 3D sub-blocks and store the panels. The ship maneuvers with controlling devices. Thus, interaction with the ground is detected based on information available for the rock tip location and ship position. Ship motions are encompassed in the coupling algorithm. In way of an FSI interface the rock penetration (displacement) inside the hull can be determined and the structural deformation is used to compute the contact forces. The structural solver makes use of the momentum equation to estimate the contact forces and moments at the FSI interface. Ship motions are updated at each time step.

External dynamics are solved using the approach of Taimuri et al. (2020). Accordingly, the ship can be modeled as a rigid structure maneuvering in deep or shallow waters, in calm or short-wave conditions and with or without wind and ocean currents. Shallow waters have a larger influence when the water depth to ship draft ratio is between 1.5 and 1.2. A ratio of the order of 3 (or higher) corresponds to deep water conditions (Vantorre et al., 2017). According to HELCOM – Helsinki Commission (2021) grounding statistics, sea depths range from 10 to 500 m in areas where grounding occurred. The grounding accidents of Exxon Valdez and Costa Concordia indicate that both deep and shallow sea conditions should be considered when assessing grounding risk. Notwithstanding this, the present study considers only the case of a deep-water scenario.

FSI is governed by the rock’s tip and the triangular hull panels. To idealize the physics of plate tearing the hull panels were stored in identical sub-blocks specified by 3D Cartesian coordinates that bound the complete hull shape. The required sub-block can be identified directly from the coordinates of the rock point on a ship-fixed coordinate system. For those cases that the rock is located within a sub-block, a ray tracing algorithm can be used to detect the intersection of a vector heading towards the ship base (Moller and Trumbore, 1998). This modeling strategy helps to accurately estimate the distance between the hull panel and the rock tip, which may then be used to calculate contact forces. Once an intersection is detected, the structure will deform. Thus, internal mechanics make use of the so called “upper-bound theorem of plasticity” (Simonsen, 1997a; Sun et al., 2017). Output results from this numerical scheme are the ship trajectory, grounding length, absorbed energy by the ship and forces leading to deformation. Different rock geometries can be formulated based on the gap openings and flap angles of different shapes (Simonsen, 1997c,b). However, the method presented in this paper is only applicable to conical rock shapes with rounded tips.

3.1. FSI modeling assumptions

The internal mechanics model (Simonsen, 1997a; Sun et al., 2017) introduced in this paper is based on the following assumptions:

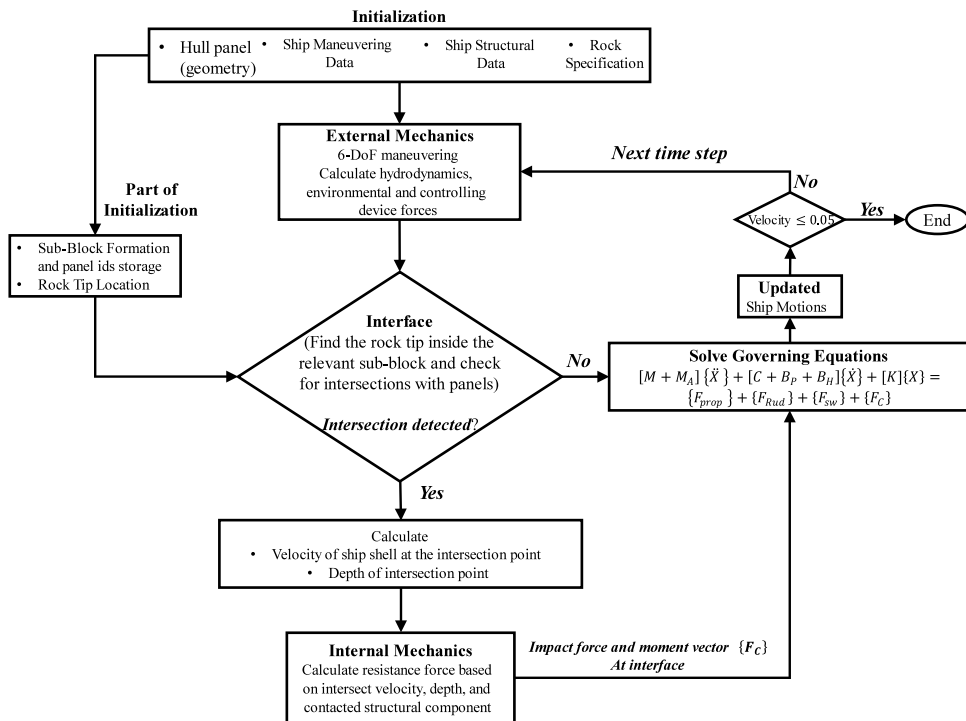


Fig. 1. Two-way coupling of ship external mechanics and internal mechanics. A simplified FSI one time step partitioned approach.

- The structural material is rigid and plastic. Accordingly, elastic deformation is neglected and von Mises yield criteria are followed;
- The rock is idealized as a cone with a rounded tip radius and a semi-apex angle;
- In the first instance, the deformation mechanism of each of the structural components is considered separately. Following this, the resistance of all structural members within the deformation zone is summed up;
- Before fracture, the plate follows a prescribed deformation mode according to which the plate wraps around the rounded tip of the cone;
- After fracture, the bottom structure of the plate conforms to the rock and the generatrix (line segment between cone base and apex of the cone) is used to define the contact force on the plate fractured;
- The plate cutting phenomena follow stable or clean curling cut. Concertina tearing and braided cut of the plate are not considered;
- Strain effects in the longitudinal direction of the plate, girder and stiffener components are not accounted for;
- The plate plastic resistance and transverse floors are modeled according to [Simonsen \(1997a\)](#), [Sun et al. \(2017\)](#) respectively. Accordingly, (i) longitudinal girders and bulkheads are unstiffened and only their membrane effects are considered; (ii) longitudinal stiffeners only account for bending deformation;
- The deformation zone ahead of the rock is defined by penetration into the hull and a cone semi-apex angle.

According to [Taimuri et al. \(2020\)](#) assumptions related to external mechanics are summarized as follows:

- In-plane hull hydrodynamic damping coefficients are based on semi-empirical expression that originates from the regression of captive model tests (CMT). Out-of-plane radiation damping is estimated using linear theory (natural period of the ship).
- Added inertia can be approximated either by a semi-empirical expression ([Brix, 1993](#); [Clarke et al., 1982](#)) or strip theory ([Frank, 1967](#); [Journée, 1992](#));
- Shallow water effects are accounted for by an increase in resistance. However, the influence of wave-making resistance, squat and bank effects are not considered;
- Added inertia and damping in shallow waters are modeled according to [Vantorre \(2001\)](#) Heave and pitch motions are not considered;
- Short waves account for mean 2nd order wave drift forces ([Faltinsen, 1990](#); [Faltinsen et al., 1980](#); [Sakamoto and Baba, 1986](#)). The effect of limiting water depth on the 2nd order mean drift force is defined according to [Longuet-Higgins \(1977\)](#).

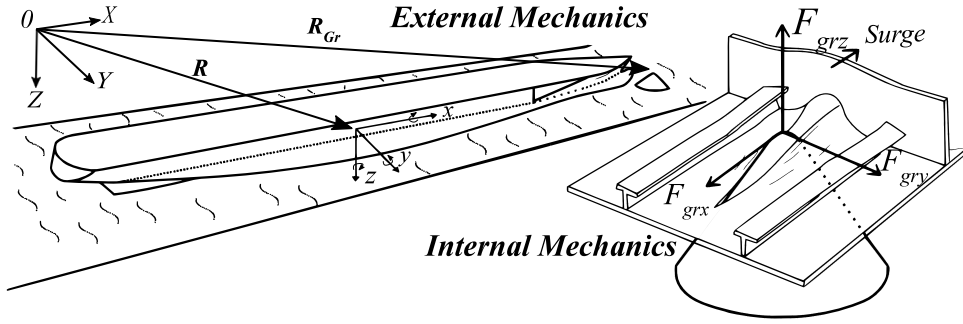


Fig. 2. Illustration of a hard grounding scenario over a conical rock during ship maneuvering.

LS-DYNA simulations assumed that all structural components are made of mild steel (S235). Plates were modeled by 6 - DoF shell elements with Belytschko–Tsay formulation (LSTC, 2021) and the Hughes–Liu degenerative continuum model was used to model stiffeners, girders and frames (LSTC, 2021). Based on the convergence study of Kim et al. (2022b, 2021), element sizes of the order of 150 mm and 100 mm were considered satisfactory in terms of idealizing the bottom plate tearing for the passenger ship and the box barge models respectively. The Cowper–Symonds equation was applied to model strain effects (Jones, 2011). As part of this process, uncertainties of relevance to the estimation of the dynamic fracture strain factor have been thoroughly considered. According to Paik et al. (2017), the dynamic fracture strain rate for mild steel is around 0.07 for 14.5 mm plate thickness and 191 mm of element size. Thus, for the topology considered in this paper the fracture strain factor would be around 0.087–0.093. On the other hand, Lehmann et al. (2001) empirical formulae suggests a fracture strain of 0.11–0.12. In conclusion, an average fracture strain of the order of 0.1 was considered adequate (Kim et al., 2021).

The external mechanics model used in LS-DYNA–MCOL coupling simulates the case of a 6-DoF rigid ship heading straight with an initial forward speed in deep and calm waters. The added mass has been considered to remain constant at infinite frequency. Hydrodynamic radiation damping with memory effects were accounted for. The simplified 6-DoF maneuvering model used the same (infinite frequency) added inertia coefficient and ship heading with forward speed. However, it did not account for the influence of controlling devices and resistance effects. In-plane hull hydrodynamic forces were modeled according to Taimuri et al. (2020) and out-of-plane linear damping was evaluated as described in Appendix A.

3.2. External mechanics

The coordinate systems used for (i) the idealization of ship dynamics and (ii) the direction of structural deformation forces due to the penetration of the rock into the hull are shown in Fig. 2. Ship motions were defined using the Earth fixed inertial coordinate system $\bar{R} = [X, Y, Z]$ associated with the navigational position of the vessel. The body-fixed coordinate system ($r_0 = \{x, y, z\}$) was attached to the intersection of the plane passing through the waterplane area amidships the symmetric hull (Taimuri et al., 2020). The rock was specified as a point node, in the inertia coordinate system $\bar{R}_{Gr} = [X_{Gr}, Y_{Gr}, Z_{Gr}]$.

The governing equation of ship dynamics (Fossen, 2011; Matusiak, 2021; Taimuri et al., 2020), structural deformation (Simonsen, 1997a; Sun et al., 2017) and contact detection is:

$$[M + M_A] \{\ddot{X}\} + [C + B_p + B_H] \{\dot{X}\} + [K] \{X\} = \{F_{prop}\} + \{F_{Rud}\} + \{F_{sw}\} + \{F_C\} \quad (1)$$

where, $\ddot{X} = \{\dot{u}, \dot{v}, \dot{w}, \dot{p}, \dot{q}, \dot{r}\}^T$, $\dot{X} = \{u, v, w, p, q, r\}^T$ and $X = \{x, y, z, \phi, \theta, \psi\}^T$ are acceleration, velocity, and position vectors (translational and angular) in the body-fixed coordinate system; M and M_A are the inertia and added inertia matrix respectively; C is rigid-body Coriolis and centripetal forces and moment matrix showing the rotation of the body in the inertial frame as the ship's origin r_0 is at a distance $\bar{r}_G = [x_G, y_G, z_G]$ away from the center of gravity; B_p is the radiation damping matrix, B_H is hydrodynamic linear and higher-order coefficients considering viscous damping, K is the restoring forces and moment matrix; F_{prop} , F_{Rud} , and F_{sw} are the contributions of propeller, rudder, and short waves respectively. The contact forces and moments are defined by the vector F_C . The details of inertia, Coriolis, centripetal, restoring forces and the damping matrix are given in Appendix A.

Structural deformations were coupled with 6-DoF ship external dynamics model via a contact detection algorithm (see Section 3.4). The governing 2nd order non-linear differential Eq. (1) was numerically solved using the 4th order Runge–Kutta time-stepping scheme. The response of the ship was calculated in the body-fixed coordinate system. To transfer the response into the global/Earth-fixed coordinate system the transformation matrix $T(\gamma)$ shown in Eq. (2), was utilized:

$$T_T(\gamma) = \begin{bmatrix} \cos(\psi) \cos(\theta) & \cos(\psi) \sin(\theta) \sin(\phi) - \sin(\psi) \cos(\phi) & \cos(\psi) \sin(\theta) \cos(\phi) + \sin(\psi) \sin(\phi) \\ \sin(\psi) \cos(\theta) & \sin(\psi) \sin(\theta) \sin(\phi) + \cos(\psi) \cos(\phi) & \sin(\psi) \sin(\theta) \cos(\phi) - \cos(\psi) \sin(\phi) \\ \sin(\theta) & \cos(\theta) \sin(\phi) & \cos(\theta) \cos(\phi) \end{bmatrix} \quad (2)$$

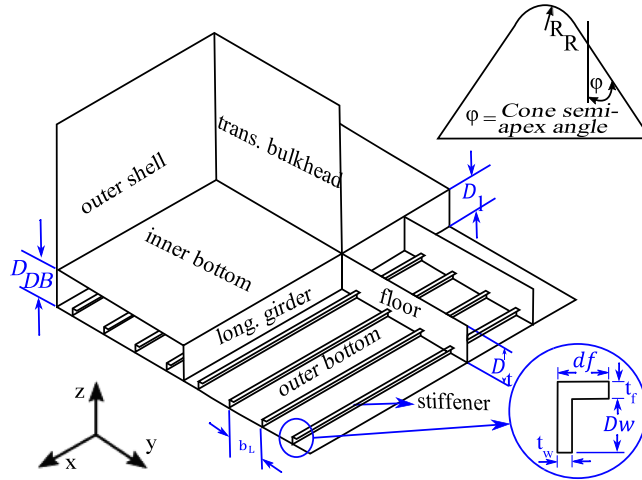


Fig. 3. Idealization of ship bottom structure and conical rock.

$$\mathbf{T}_R(\boldsymbol{\gamma}) = \begin{bmatrix} 1 & \sin(\phi) \tan(\theta) & \cos(\phi) \tan(\theta) \\ 0 & \cos(\phi) & -\sin(\phi) \\ 0 & \frac{\sin(\phi)}{\cos(\theta)} & \frac{\cos(\phi)}{\cos(\theta)} \end{bmatrix}$$

where $\boldsymbol{\gamma}$ represents Euler angles, $\mathbf{T}_T(\boldsymbol{\gamma})$ is the transformation matrix of translational velocities from body coordinate system to inertial coordinates and $\mathbf{T}_R(\boldsymbol{\gamma})$ is a transformation matrix of angular velocities into the inertial coordinate system.

In shorter notation Eq. (2) this can be written as Manderbacka et al. (2015), Matusiak (2021):

$$\dot{\mathbf{X}} = \begin{bmatrix} \mathbf{T}_T(\boldsymbol{\gamma}) & \mathbf{0}_{3 \times 3} \\ \mathbf{0}_{3 \times 3} & \mathbf{T}_R(\boldsymbol{\gamma}) \end{bmatrix} \dot{\mathbf{x}} \quad (3)$$

3.3. Internal mechanics

The contact force \mathbf{F}_C (see Eq. (1)) results from impact loads. In the models of Simonsen (1997a) and Sun et al. (2017) the energy dissipation is estimated by integrating the stress and strain field over the volume of the structure to form an analytical equation. The structural resistance force presented in Eq. (4) reflects the energy balance in way of grounding contact; i.e. it expresses the relationship that the rate at which energy dissipates internally by plastic deformation, friction, and by fracture must be equal to the external work done.

$$F_H U = \dot{E}_p + \dot{E}_c + \dot{E}_f = F_p \cdot U + \int_S p \mu U_{rel} dS \quad (4)$$

where, F_H is the resisting force of the structure in the direction of U ; U is the relative velocity between the ship and a rock; \dot{E}_p , \dot{E}_c , \dot{E}_f express the rate of plastic, crack, and frictional energy dissipation respectively; F_p is the plastic resistance which includes both plasticity and fracture; μ is the Coulomb coefficient of friction; The last term of Eq. (4), represents the sliding energy dissipation due to normal and frictional forces in way of the contact surface of the rock and the plate (p is the plate's normal pressure on the rock based on contact area S between rock and plate; U_{rel} is the relative velocity between rock and plate according to Simonsen, 1997a).

Hard grounding was assumed to take place over the rigid conical rock with a rounded tip radius R_R and a semi-apex angle ϕ (see Fig. 3). The forces generated by the individual structural components were summed up to produce the resultant contact forces. The hull outer shell holds the structural components (floors, girders, bulkheads, and stiffeners) which are attached to the shell plate. Therefore, the global mode of deformation is governed by the outer hull plating, where the intersections are assumed to be intact during the deformation process. The generalized deformation modes and plate openings following grounding can be idealized as shown in Fig. 4. The membrane strain can be defined by the longitudinal and transversal gap openings u_0 and v_0 respectively (Simonsen, 1997a). A summary of the plate opening, extent of deformation, fracture penetration and structural component forces are presented in Appendices B and C.

The horizontal and vertical reaction forces were evaluated by utilizing the plastic force, rock geometry and plate split angle. The effect of friction “ g ” and vertical to horizontal force ratio “ k ” were defined for both intact and fractured hull plating (Simonsen, 1997c). Eq. (5) shows the horizontal to plastic force ratio and vertical to horizontal force ratio

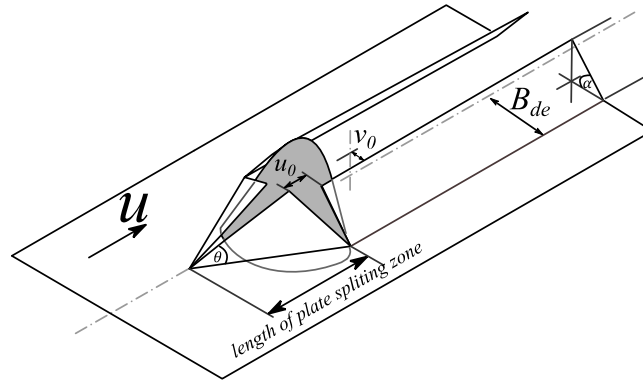


Fig. 4. Plate membrane and bending deformation during grounding.

estimation for the intact plate. Eq. (6) represents fractured plate.

$$g = \frac{F_H}{F_P} = \left(1 - \frac{\mu}{\sin \frac{\psi_C}{2} + \mu \cos \frac{\psi_C}{2}} \right)^{-1}, \quad k = \frac{F_V}{F_H} = \frac{1 - \mu \tan \frac{\psi_C}{2}}{\mu + \tan \frac{\psi_C}{2}} \quad (5)$$

$$g = \frac{F_H}{F_P} = \left(1 - \frac{\mu}{\cos \phi \sin \theta + \mu \cos \theta \cos \xi} \right)^{-1} \quad (6)$$

$$k = \frac{F_V}{F_H} = \frac{\sin \phi - \mu \cos \phi \sin \xi}{\cos \phi \sin \theta + \mu \cos \theta \cos \xi}$$

where, μ is the coefficient of friction, ξ is the rolling of the plate and θ is the plate split angle.

The plate split angle represents the extent of plate deformation ahead of the conical rock. It helps demonstrate how far the length of the plate opening shall propagate before reaching a plastic zone. The plate split angle relies on structural component deformation energy and is critical in terms of suitably idealizing damage extents (see Eqs. (5)–(6)).

3.3.1. Plate split angle idealization

In Simonsen (1997a) the plate split angle θ (see Fig. 4) was defined as an unknown parameter that remains constant and minimizes the total resistance force of the structure. The plate split angle depends on the geometry of the indenter (rock). For instance, splitting of a plate can be assumed as the semi-angle of the wedge when using a wedge-shaped indenter. However, the splitting of a plate over a conical rock can vary depending on the depth of penetration and the actual shape. The following discussion highlights the importance of properly evaluating the plate split angle by demonstrating a comparison of plate split angle obtained from FEM solver against the theoretically minimized resistance force approach introduced by Simonsen (1997a).

Fig. 5, illustrates the bare plate splitting angle approximated by the simplified (Simonsen, 1997a) model at different penetration depths with a cone semi-apex angle of 45° . Fig. 6, shows the more detailed LS-DYNA FEA simulations with 2 m depth and cone semi-apex angle of 45° . In the examined scenarios for LS-DYNA simulations the rock was assumed to be rigidly fixed in all directions and surge translations were applied at the side shells of the box (or plate). Plate specifications are presented in Appendix E. The bare plate split angle varied between 34° to 48° , depending on the time and position of the rock. The corresponding plate split angle at 2 m of rock penetration was around 6° (see Fig. 5 encircled region). This value deviates quite significantly from FEM simulations and helps underline the importance of accurate split angle approximations.

To examine the effect of structural details on the variation of the split angle, a simple bare-plate and a complete box-ship structure model comprising of double bottom, center girder, stiffeners, plate, and floors were simulated in LS-DYNA (see Fig. 7a, b) for the scenario presented in Appendix E. The original data was extracted at different positions along the length of the structure, where the velocity of the structure drops lengthwise. Simulations have been categorized by the base radius of the cone, height of the cone (penetration) and cone semi-apex angle. Fig. 7a, b show that the variation of a bare plate split angle is less sensitive to the speed drop of the plate in comparison to a fully structured ship. In a bare plate, the values are close to each other irrespective of cone geometry and penetration depth. Notwithstanding this, slightly more disperse data for a few categories were observed in full hull forms (e.g., $\delta_{out} = 1$ m corresponds to $\phi = 45^\circ$, while $\delta_{out} = 2$ m corresponds to $\phi = 27^\circ$).

A summary of the results of LS-DYNA simulations is illustrated in Fig. 8. The minimum and maximum plate split for a bare plate are 26° and 56° respectively. For a complete box-structured ship these values become 32° and 63° (see Fig. 8). The mean variation of the plate rolling angle ranged from 0.56–0.72 times the plate split angle. These values can be used for estimating ξ . Theoretically the bound of the plate rolling ξ due to the relative velocity of the ship and contact surface

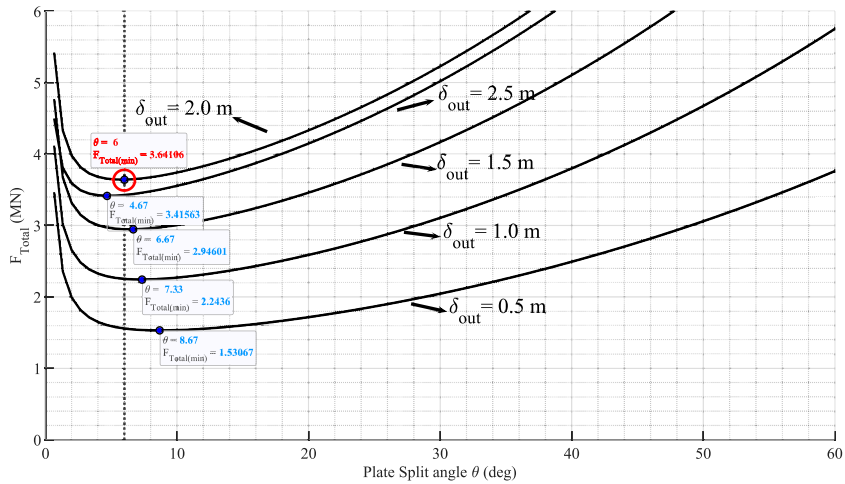


Fig. 5. Theoretical total resistance force of bare plate as a function of the split angle at different penetration depth, cone semi-apex angle of 45°.

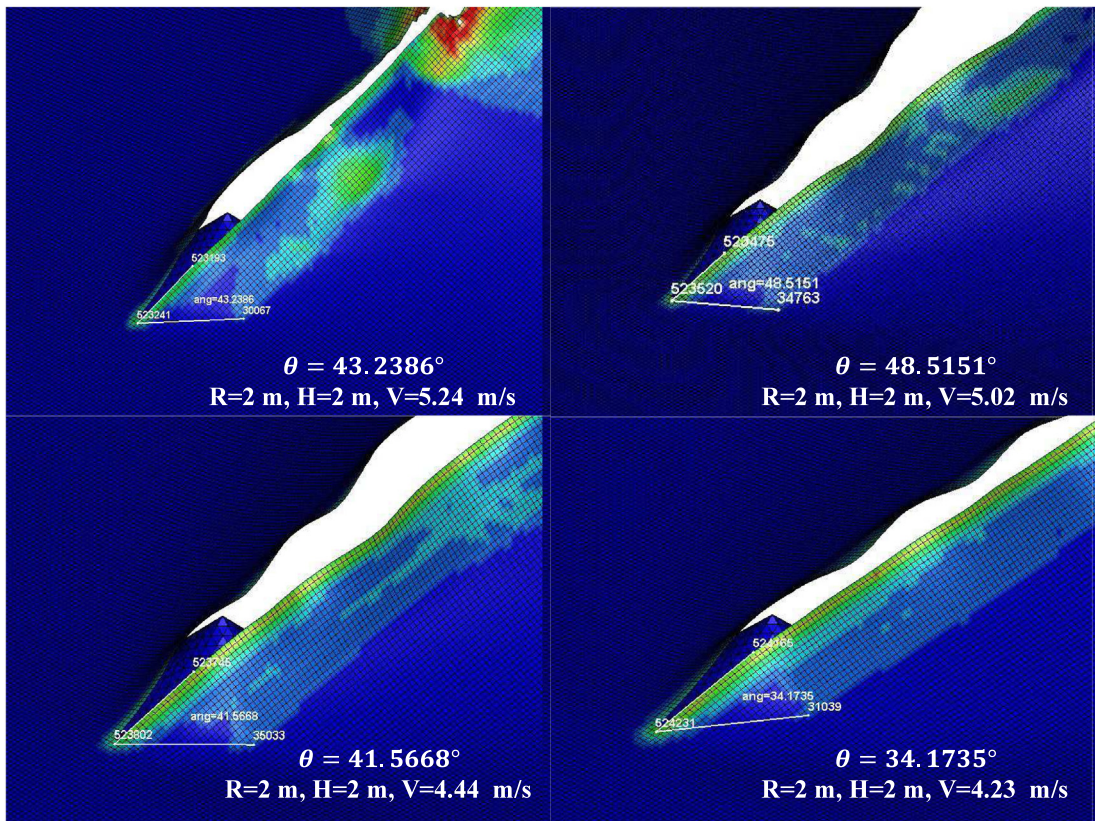


Fig. 6. Variation of bare plate split angle, computation from LS-DYNA with the body-fixed condition. Cone semi-apex angle of 45°.

is in between 0 and θ (Simonsen, 1997a). For ease of use, in the present analysis plate rolling was assumed to be 0.5 times the plate splitting angle ($\xi = 0.5\theta$). These simulations underline the fact that, the approach proposed by Simonsen (1997a) which selects a plate split angle at minimum resistance force, leads to significant underestimation of the plate split angle as compared to FEA simulations.

The curve fitting of the plate split angle as a function of penetration into the hull and radius of the cone base is presented in Eq. (7) and Fig. 9. The curve fitting method used to determine the plate split angle has been formulated as a function of B_{de} and δ_{out} . As part of this process a complete ship model and average values of the plate split angle were

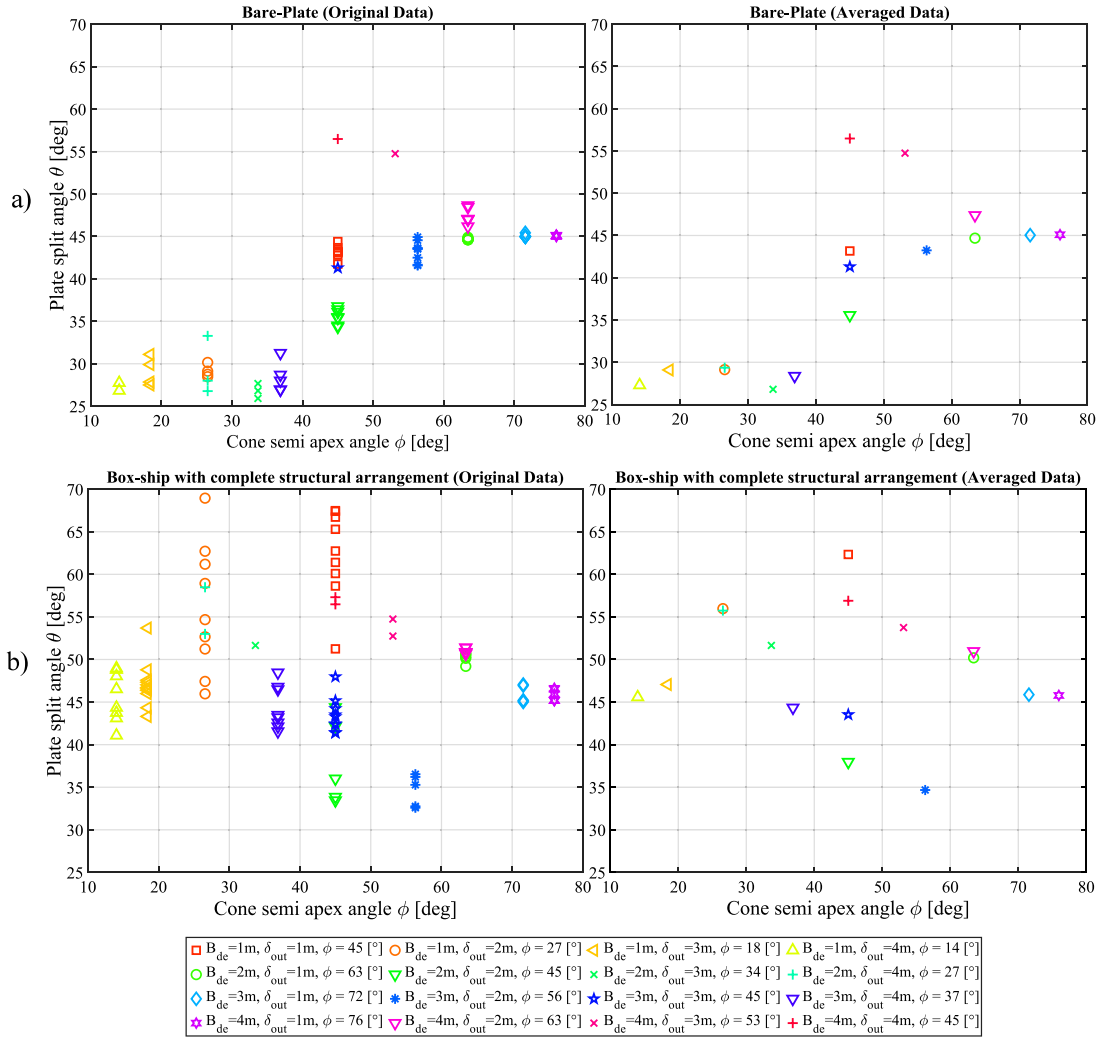


Fig. 7. Data of plate split angle as a function of cone semi-apex angle, penetration into the hull δ_{out} and base-radii B_{de} of the rock from FEM simulation. (a) bare plate split angle, (b) box-ship complete structural arrangement.

considered. The averaged data from the combination of different rock bases and penetrations are illustrated in Fig. 7b. Polynomial curve fitting of the 3rd order for δ_{out} values in way of the base of the cone were implemented according to the equation:

$$\theta(\delta_{out}, B_{de} \{i\}) = a_i \delta_{out}^3 + b_i \delta_{out}^2 + c_i \delta_{out} + d_i : i \in \{1, 2, 3, 4\} \quad (7)$$

where, $a, b, c,$ and d are the coefficients of the polynomial equation, i subscripts correspond to the four different rock base radii. These four different curves were fit according to Eq. (8), as a function of the rock base radii B_{de} (see Fig. 9 – bottom).

$$\begin{cases} a = P_{1a}B_{de}^3 + P_{2a}B_{de}^2 + P_{3a}B_{de} + P_{4a} \\ b = P_{1b}B_{de}^3 + P_{2b}B_{de}^2 + P_{3b}B_{de} + P_{4b} \\ c = P_{1c}B_{de}^3 + P_{2c}B_{de}^2 + P_{3c}B_{de} + P_{4c} \\ d = P_{1d}B_{de}^3 + P_{2d}B_{de}^2 + P_{3d}B_{de} + P_{4d} \end{cases} \quad (8)$$

Back substitution of the polynomial coefficients of Eq. (8) into Eq. (7) resulted in a split angle θ expressed as a function of B_{de} and δ_{out} . This new equation of plate split angle helped simulate the dynamic behavior of the ship structure as a function of conical rock geometry. The model is an improved version of the previously considered average value for the entire ship introduced by Simonsen (1997a) and, depending on penetration indentation, may lead to different horizontal and vertical forces (see Eq. (6)).

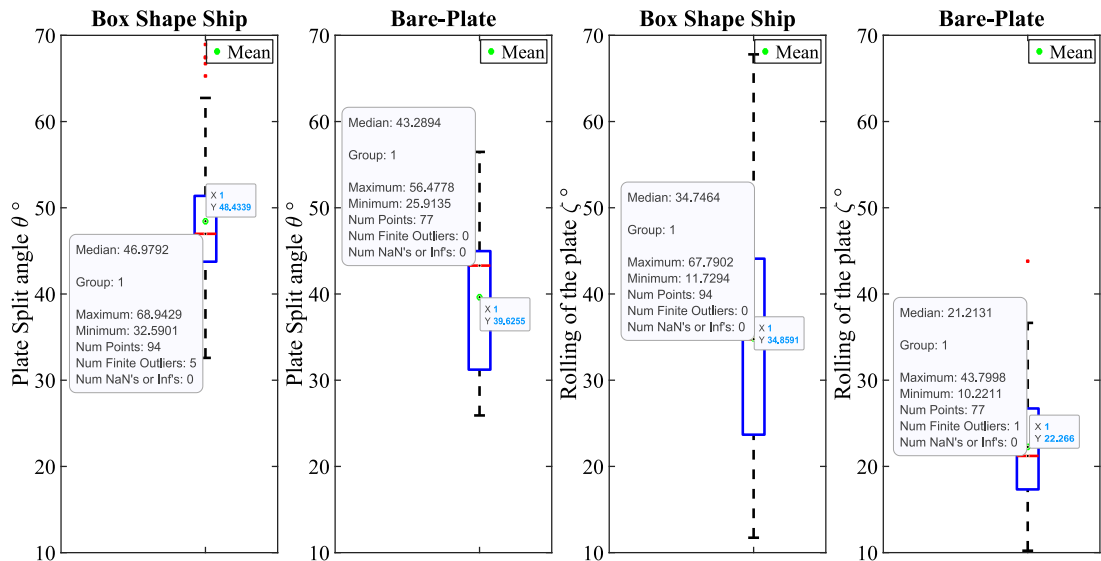


Fig. 8. Distribution of numerically computed plate split angle and plate rolling angle of fully structured ship and bare plate.

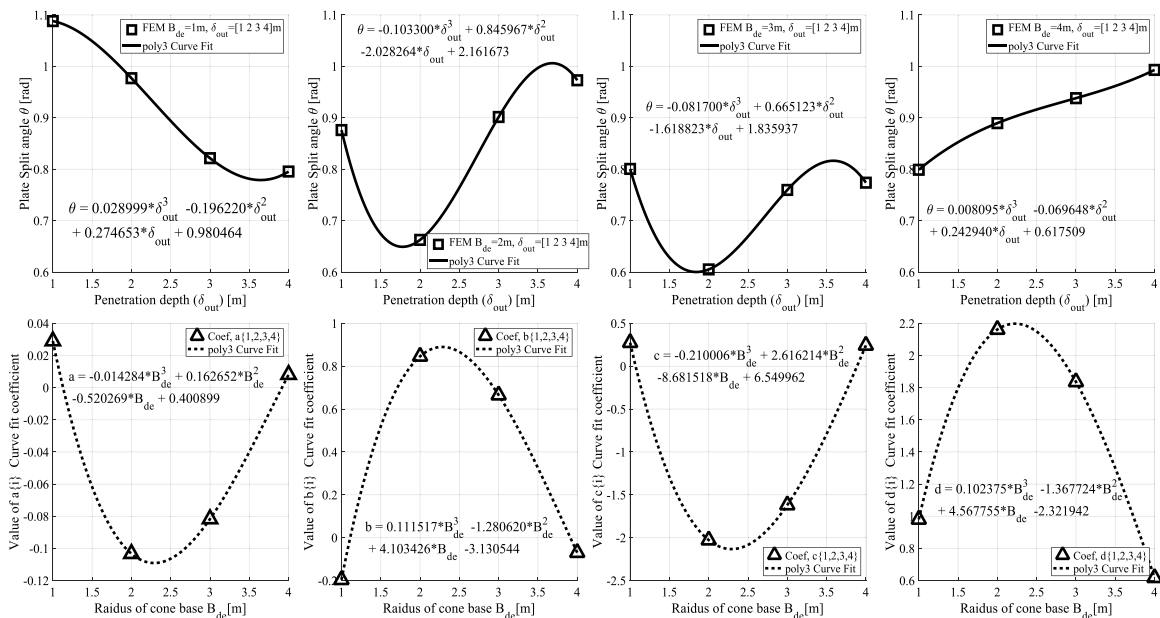


Fig. 9. Curve fitted expression of plate split angle as a function of rock geometry.

3.4. Contact detection algorithm

To ensure appropriate modeling of the penetration into the hull and rapid simulation of the grounding event, a fast contact detection algorithm has been developed. This algorithm produced the penetration depth from which the structural deformation was calculated at each time step. The implementation of the method is illustrated in Figs. 10, 11. The rigid hull model was idealized by triangular panels. The coordinates of each panel were defined from the ship's origin (see Fig. 2). The key steps of the algorithm are summarized as follows:

Based on the ship's main dimensions a ship bounding cartesian grid that consists of identical 3D sub-blocks (G_x , G_y , and G_z along the length, beam, and depth of the ship respectively) is generated (cartesian grid initialization in

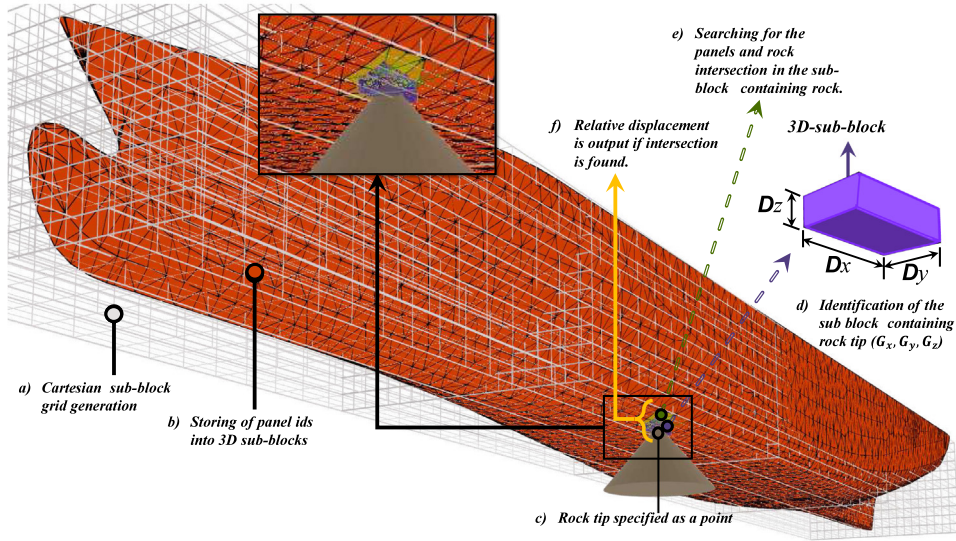


Fig. 10. A general illustration of the method followed for rapid evaluation of contact detection, showing coupling of ship structure and hydrodynamics.

- (a) Fig. 11);
- (b) The number of panels in respective 3D sub-blocks are identified, and the indices of these hull panels are stored (the process of allocation of panel IDs in each sub-block is demonstrated in Fig. 11);
- (c) Fig. 11);
- (d) The rock tip is idealized as a point in an inertial coordinate system represented by a vector \vec{R}_{Gr} (Fig. 2). The coordinates of this point are transformed into the body-fixed coordinate system, while the search of the rock within the sub-block is conducted in the ship fixed coordinate system;
- (e) The position vector from the ship origin to the rock tip is used to determine whether the rock is within the ship's bounding cartesian grid or not. If the rock tip is inside the cartesian grid, a 3D sub-block that contains the rock tip is identified Fig. 10. Otherwise, the solver returns to the equation of motion depicted in Fig. 11.
- (f) If the rock tip is located inside the 3D sub-block, the next step is to locate the intersection between panels and the tip of the rock. If there are no panels in a sub-block containing the rock tip, then neighboring blocks in the direction of the rock tip to the base are searched until an intersection with a sub-block grid is detected and stored. The depth of the penetration is calculated by a ray-tracing algorithm (Badouel, 1990; Moller and Trumbore, 1998).
- (g) After the intersection is identified, the penetration into the hull δ_{out} , is output from the contact coupling model. This penetration is then transferred to the internal mechanics model to evaluate the forces leading to structural deformation.

The contact force on individual structural members in way of an intersection depends on the penetration and details of structural members at the location of the rock–ship interaction. The horizontal force F_H is decomposed into the longitudinal and lateral components by using the relative velocity between rock and ship intersection panel. The velocity of the ship shell at the intersection point is calculated from the velocity vector field equation:

$$\vec{V}_{int} = \vec{V} + \vec{\omega} \times \vec{r}_{int} \quad (9)$$

where, $\vec{V}_{int} = [u_{int}, v_{int}, w_{int}]$ is the velocity of the panel at the intersection point; $\vec{V} = [u, v, w]$ is the body velocity of the ship, $\vec{r}_{int} = [x_{int}, y_{int}, z_{int}]$ depicts the intersection position of the rock from ship origin and $\vec{\omega} = [p, q, r]$ is the angular velocity of the body. These velocities refer to the location of the rock and panel intersections, which are in a body-fixed coordinate system. The velocities are then transformed to the global coordinate system via the transformation matrix:

$$\begin{Bmatrix} u_{global} \\ v_{global} \\ w_{global} \end{Bmatrix} = T_T(\gamma) \begin{Bmatrix} u_{int} \\ v_{int} \\ w_{int} \end{Bmatrix} \quad (10)$$

The components of longitudinal, lateral, and vertical force components in the global coordinate system are defined as:

$$F_{Txc,global} = -\frac{u_{global}}{\sqrt{u_{global}^2 + v_{global}^2}} F_H,$$

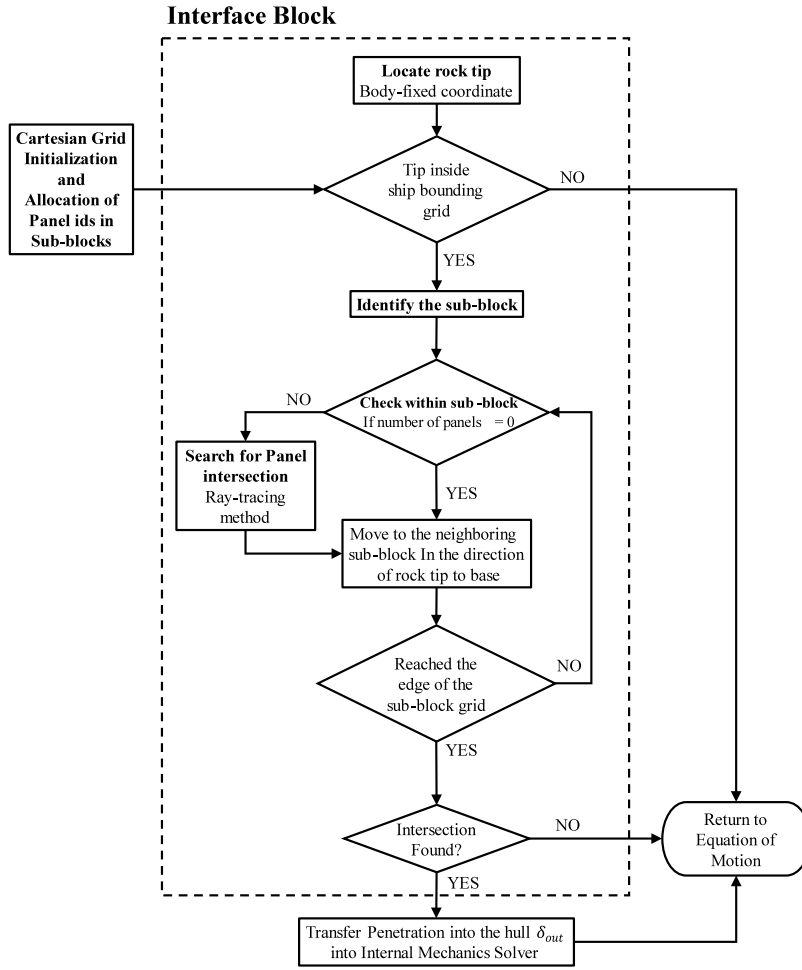


Fig. 11. The procedure of the contact search algorithm.

$$F_{TYc,global} = -\frac{v_{global}}{\sqrt{u_{global}^2 + v_{global}^2}} F_H, \quad (11)$$

$$F_{TZc,global} = -F_V$$

In the above expression, the negative signs in the longitudinal and lateral planes express the relative velocity between the ship panel and rock. The total force is the sum of plastic plus fracture and frictional forces (see Eq. (4)). The breakdown of the total force into plastic resistance force (plasticity and fracture) and frictional force of the structural member is given in Eqs. (12)–(13).

Plastic contact force,

$$F_{PXc,global} = -\frac{u_{global}}{\sqrt{u_{global}^2 + v_{global}^2}} (F_P),$$

$$F_{PYc,global} = -\frac{v_{global}}{\sqrt{u_{global}^2 + v_{global}^2}} (F_P), \quad (12)$$

$$F_{PZc,global} = -k * (F_P)$$

Frictional contact force,

$$F_{FXc,global} = -\frac{u_{global}}{\sqrt{u_{global}^2 + v_{global}^2}} (F_H - F_P),$$

$$F_{FYc,global} = -\frac{v_{global}}{\sqrt{u_{global}^2 + v_{global}^2}}(F_H - F_P), \quad (13)$$

$$F_{FZc,global} = -k * (F_H - F_P)$$

The origin of the plastic resistance force F_P is demonstrated in [Appendix B](#) and the total horizontal and vertical forces are given in Eqs. (5) and (6) respectively. The total contact forces displayed by Eq. (11), in the body-fixed coordinates at the point of intersection, are expressed as:

$$\begin{Bmatrix} F_{grx} \\ F_{gry} \\ F_{grz} \end{Bmatrix} = T_T^{-1}(\gamma) \begin{Bmatrix} F_{TXc,global} \\ F_{TYc,global} \\ F_{TZc,global} \end{Bmatrix} \quad (14)$$

After the transformation of the forces to the body-fixed coordinate system, the contact forces become:

$$\{F_C\} = \begin{Bmatrix} F_{grx} \\ F_{gry} \\ F_{grz} \\ F_{grz} \cdot y_{int} - F_{gry} \cdot z_{int} \\ F_{grx} \cdot z_{int} - F_{grz} \cdot x_{int} \\ F_{gry} \cdot x_{int} - F_{grx} \cdot y_{int} \end{Bmatrix} \quad (15)$$

4. Results and discussion

4.1. Input details for validation cases

The FSI model presented in Section 3 of this paper has been numerically validated via direct comparison with LS-DYNA-MCOL simulations. Results were compared against the constant plate split angle approach of [Simonsen \(1997a\)](#). Two study cases corresponding to (a) a simplified box-shaped ship and (b) the modern passenger vessel FLOODSTAND SHIP B (FSB) ([Luhmann, 2009](#)) were considered. The sub-cases of centerline and off-center (B/4) grounding were explicitly studied to better understand grounding dynamics under realistic scenarios. The plate split angle (present model and Simonsen approach), structural details, rock parameters, and ship initial conditions of box-shaped and passenger vessels are summarized in [Table 2](#). Models of the box-like and passenger ships are shown in [Fig. 12](#).

In the box-like ship model plate thickness and spacing of the floors were assumed to remain constant. Double bottom and uniform structural arrangements had only a centerline longitudinal girder. The passenger ship model consisted of more comprehensive and varying structural details namely different plate thicknesses, double bottom heights and location of the longitudinal girder (see [Fig. 13](#)). This variation was idealized in the simplified FSI model by dividing the ship into 6 longitudinal sections and by specifying structural details as illustrated in [Fig. 13](#). The results presented in the following sections follow the coordinate setup adopted by LS DYNA as depicted in [Fig. 12](#). The origin of the ship was assumed to lie on the center of gravity. The velocity transformation from the maneuvering model coordinates ([Taimuri et al., 2020](#)) to LS-DYNA coordinate system is presented in [Appendix D](#). It is noted that the MCOL-LSDYNA coupling accounted only for heave, roll, and pitch restoring forces (see Eq. (5)). Therefore, in the validation study the effects of surge, sway and yaw motions in the restoring forces matrix (\mathbf{K}) of [Appendix A](#) were ignored. The input details for MCOL simulations are given in [Appendix F](#).

4.2. Numerical validation of a box-shaped ship centerline grounding

The time history of ship motions, sliding forces, and deformation energy of the centerline grounding case are summarized in [Figs. 14–16](#). The top three plots in [Fig. 14](#), represent the surge, heave, and pitch velocities of the ship. The bottom three figures depict their respective displacements. The longitudinal damage extents evaluated when using the present simplified FSI method were 4.8% shorter than those evaluated by LS-DYNA simulations. This resulted in marginally different damage lengths (36.80 m for FSI versus 38.65 m for LS-DYNA). On the other hand, surge velocity trends predicted by the simplified FSI and LS-DYNA simulation matched well. The slight shift of the slope in surge velocity after 2 s (see [Fig. 14](#)) reflects that as the ship is moving up, the penetration into the hull reduces, eventually leading to reduction of the longitudinal resistance force of the structure (see [Fig. 15](#)). Subsequently, the surge velocity slope changes when the ship starts to heave down after 4 s, and the longitudinal and vertical structural resistance increases. The values for heave and pitch motions of the simplified FSI model are higher in comparison to LS-DYNA simulation. This is because of the higher (i.e., more conservative) estimation of the forces by the simplified structural deformation model. At around 0.4 s the ship experiences the largest vertical force of 4.91 MN which leads to a higher heave response (see [Fig. 14](#)).

On average, the differences of the horizontal and vertical sliding forces predicted by the simplified FSI model and LS-DYNA are 0.6% and 20.0% respectively. At the outset of the contact, there is an abrupt jump of the forces predicted by the simplified model (see [Fig. 15](#)). In a real scenario, once the base of the rock is in contact with the hull, it progressively moves ahead to deform the structure. However, in the simplified approach introduced here, the contact is modeled based on the tip of the rock and the initial contribution of the rock base is ignored. This is explained in [Appendix G](#). The rupture

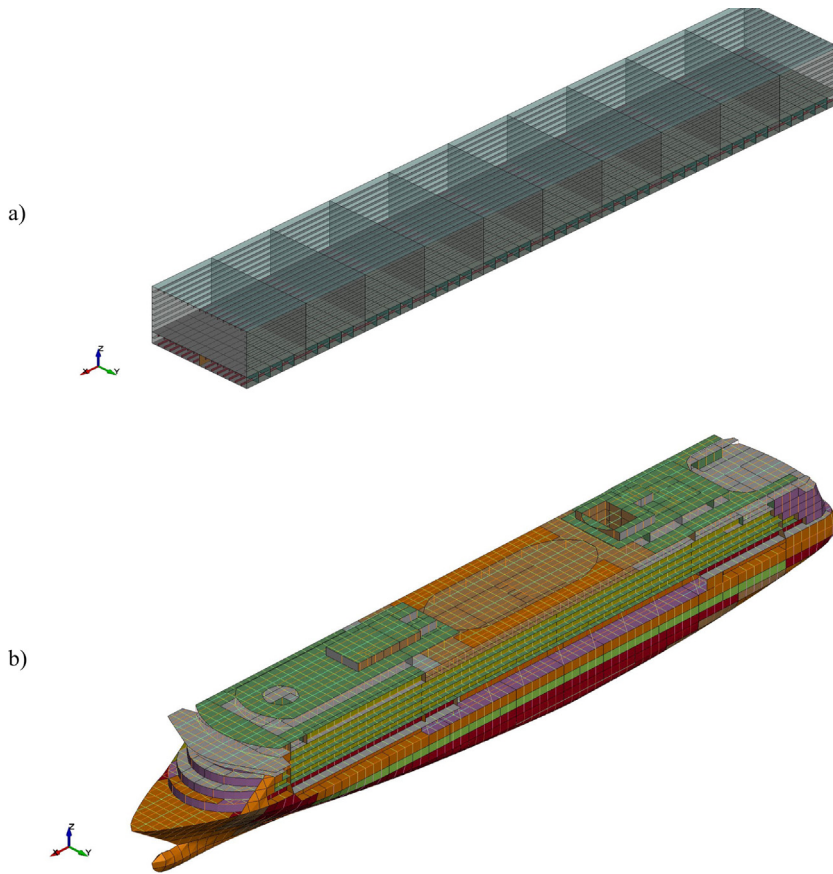


Fig. 12. Grounding case ship model. (a) Box-ship and (b) Passenger ship (Kim et al., 2021).

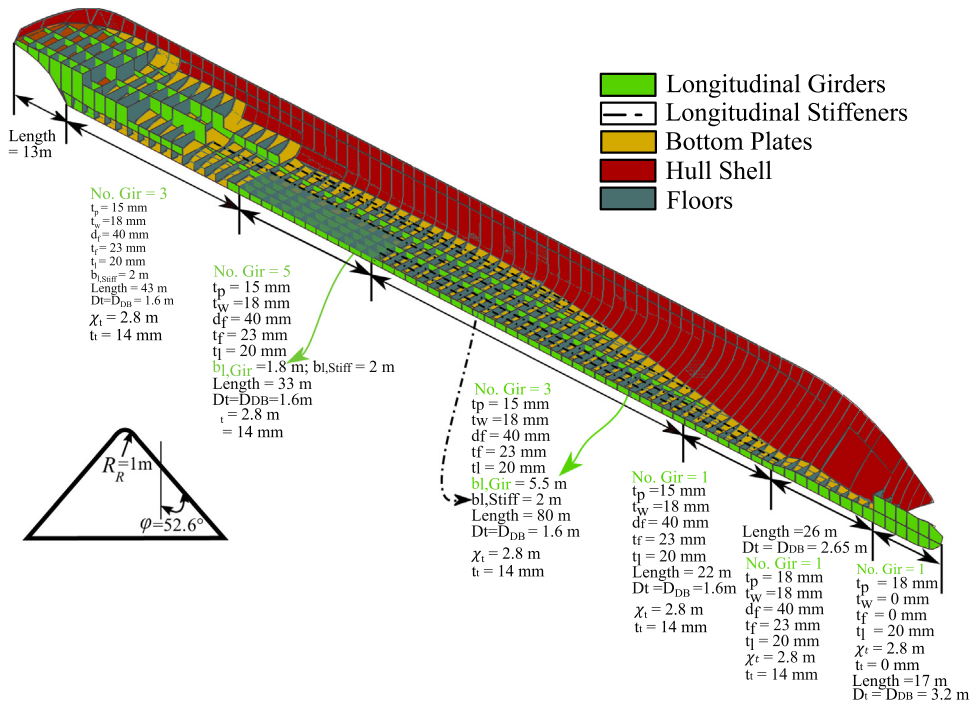


Fig. 13. Description of the structural details of a passenger ship, utilized in a simplified model.

Table 2
Main parameters of grounding simulation setup for box-ship and passenger vessel.

		Box-ship	Passenger vessel	Units
Grounding velocity	V	5.659	5.659	m/s
Ship length	L	100	216.8	m
Beam	B	16	32.2	m
Draft	T	7	7.2	m
Longitudinal CoG from origin	X_G	0	-8.8	m
Block coefficient	C_B	1	0.661	-
Vertical CoG w.r.t to ship keel (positive upward from keel)	K_G	5	15.185	m
Transverse metacentric height	G_{MT}	1.548	2.63	m
Center of flotation from CoG	X_F	0	-2.695	m
Longitudinal metacentric height	G_{ML}	117.5	543.09	m
Waterplane area	A_{wp}	1600	5950.7	m ²
Depth of the rock from the draft line		5	5.2	m
Rock tip radius	R_R	1	1	m
Semi-apex angle of cone (Rock)	ϕ	52.6	52.6	deg
Spacing between longitudinal stiffeners	b_L	1	2	m
Spacing between inner and outer bottom	D_{DB}	2	1.6	m
Width of flange	d_f	0.0	0.04	m
Height of longitudinal stiffener (height of web)	D_w	0.4	0.1	m
Height of transverse frame	D_t	2	1.6	m
Young's Modulus	E	2.058E+11	2.058E+11	Pa
Material strain hardening. Often ϵ_{cr}	n	0.1	0.1	-
Ductile fracture toughness of material	R_c	2.40E+05	2.40E+05	Pa·m
Thickness of flange	t_f	0.00	0.023	m
Web plate thickness (thickness of longitudinal girders)	t_l	0.015	0.02	m
Plate thickness	t	0.015	0.015	m
Thickness of transverse members (bulkheads, floors or frames)	t_t	0.015	0.014	m
Thickness of longitudinal web (stiffener)	t_w	0.02	0.018	m
Coulomb coefficient of friction	μ	0.3	0.3	-
Yield strength of material	σ_y	2.35E+08	2.35E+08	Pa
Flow stress of material	σ_0	2.35E+08	2.35E+08	Pa
Longitudinal spacing of transverse member	χ_t	2	2.8	m
Number of longitudinal girders		1 (center)	See Fig. 13	-
Present Simplified FSI plate split angle	θ	See Fig. 9. Eqs. (7) and (8)		deg
Simonsen approach plate split angle	θ	11	10	deg

of the transverse floor is seen as a sudden drop after each peak in the sliding force plot (see Fig. 15). The time to rupture increases as the ship velocity reduces and gets closer to zero. This behavior becomes more visible as an elongation in the force–time curve after 8 s (see Fig. 15). In the rapid FSI method proposed the deformation energy of the structure did not take into consideration the elastic behavior of the structure.

Fig. 15, presents two internal energy components namely: (a) the sliding energy that comprises normal and tangential components of the contact force (frictional force), and (b) the total energy which is the sum of absorbing and sliding energy components¹. The former is higher from the one of the simplified model and results in a 13.7% increase in results as compared to LS-DYNA. The total deformation energies predicted from both models show a rather marginal variation (less than 1%).

When the Simonsen concept of constant plate split angle is employed, the ship's longitudinal damage length increases significantly (Fig. 14). This is because the specified plate split angle lowers the total energy dissipation (Fig. 15). It reduces resistance to ship structure during grounding and prolongs the time for a ship to come to rest. The vertical sliding force obtained from Simonsen's approach (Fig. 15)¹ is slightly larger than the simplified model (Section 3.3.1). However, the overall energy decreases. This implies that the plastic resistance force is underestimated, and the frictional force is overestimated.

Table 3, compares the damage extents predicted on the basis of the simplified model and Simonsen's approach against LS-DYNA simulation. For all cases the maximum damage width is located at the beginning of the contact when the vertical force is maximum. The minimum width is obtained when the ship has the largest heave. Moreover, the inner bottom in all cases remains intact. Fig. 16(a), demonstrates the damaged hull profile that resulted from LS-DYNA simulations. Fig. 16(b) and (c), illustrate respectively the damage width, length, penetration, and resultant forces from the present method and Simonsen's approach (1997a) respectively. Fig. 16(a) and (b) show good correlation of damage length and width between the proposed model and LS-DYNA simulations. However, 61% higher estimation of the damage length is evident when choosing the method of constant plate split angle (see Fig. 16(c) and Table 3).

¹ In Fig. 15, only sliding (i.e. frictional) force is illustrated and plastic resistance is not shown. The calculation of frictional force is given in Eq. (13). However, one can see the contribution of the plastic resistance (subtracting sliding energy from total energy) from the plots of deformation energy.

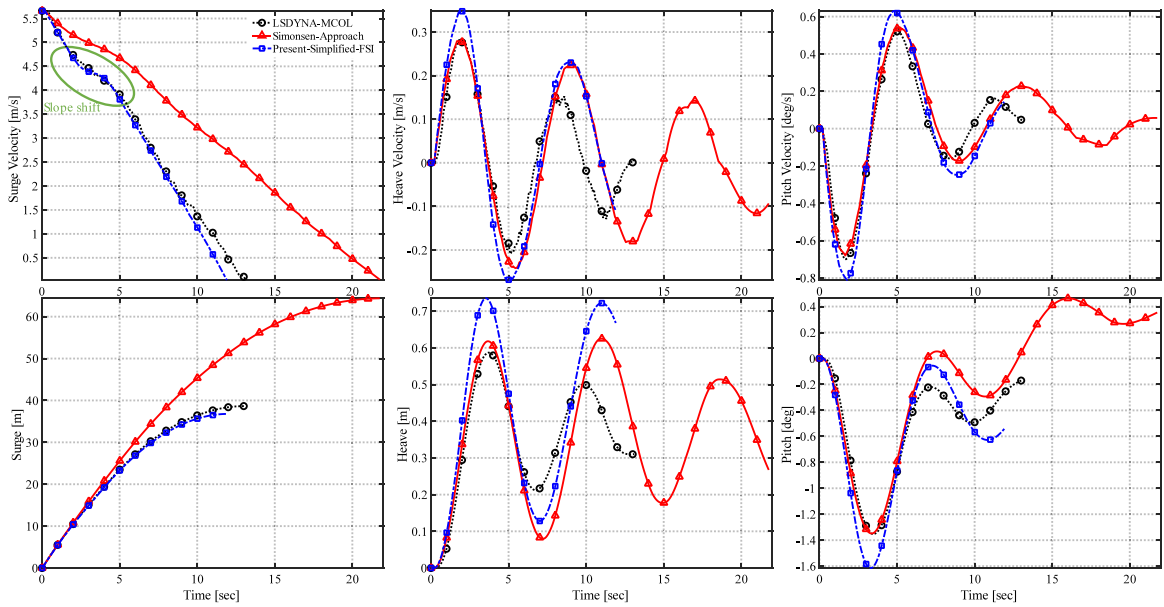


Fig. 14. Motions of centerline grounding of a box shape ship. Top velocities and bottom displacements.

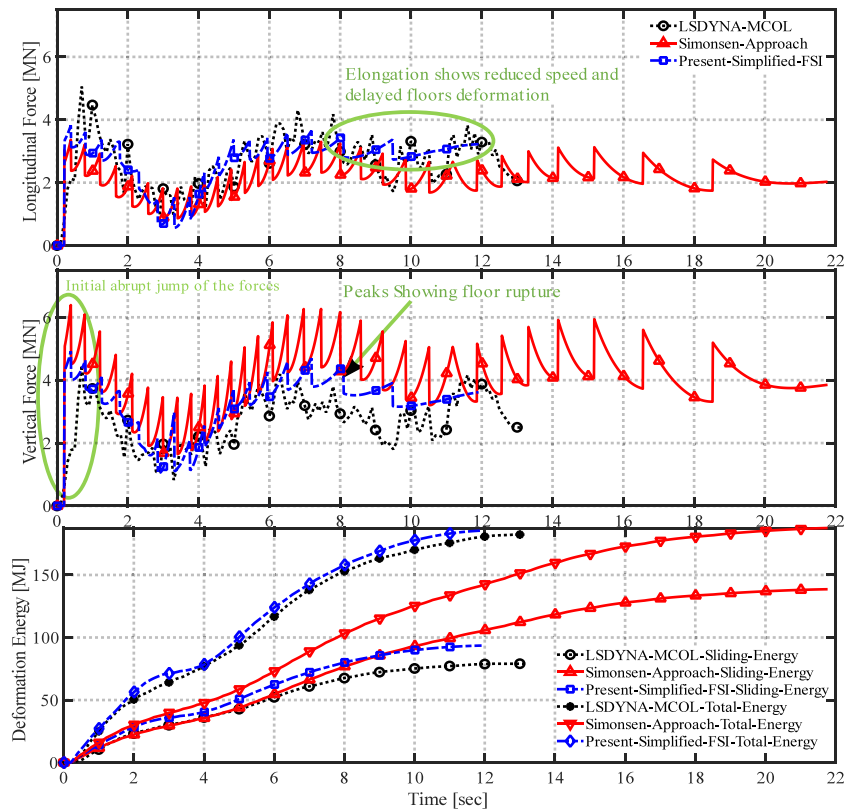


Fig. 15. Sliding grounding forces and deformation energy of centerline grounding of box shape ship.

Table 3
Centerline box-shape ship grounding. Comparison of the present model with LS-DYNA simulations.

	LSDYNA	Present model	% difference	Simonsen approach	% difference
Longitudinal extent (m)	38.65	36.80	4.78	62.47	61.63
Maximum width (m)	5.76	5.9	2.45	5.89	2.1
Minimum width (m)	1.78	1.45	18.5	2.25	26.0
Maximum penetration (m)	2.0	2.0	0	1.99	0.75
Minimum penetration (m)	0.54	0.3	44	0.60	10
Inner bottom breach	No	No	-	No	-

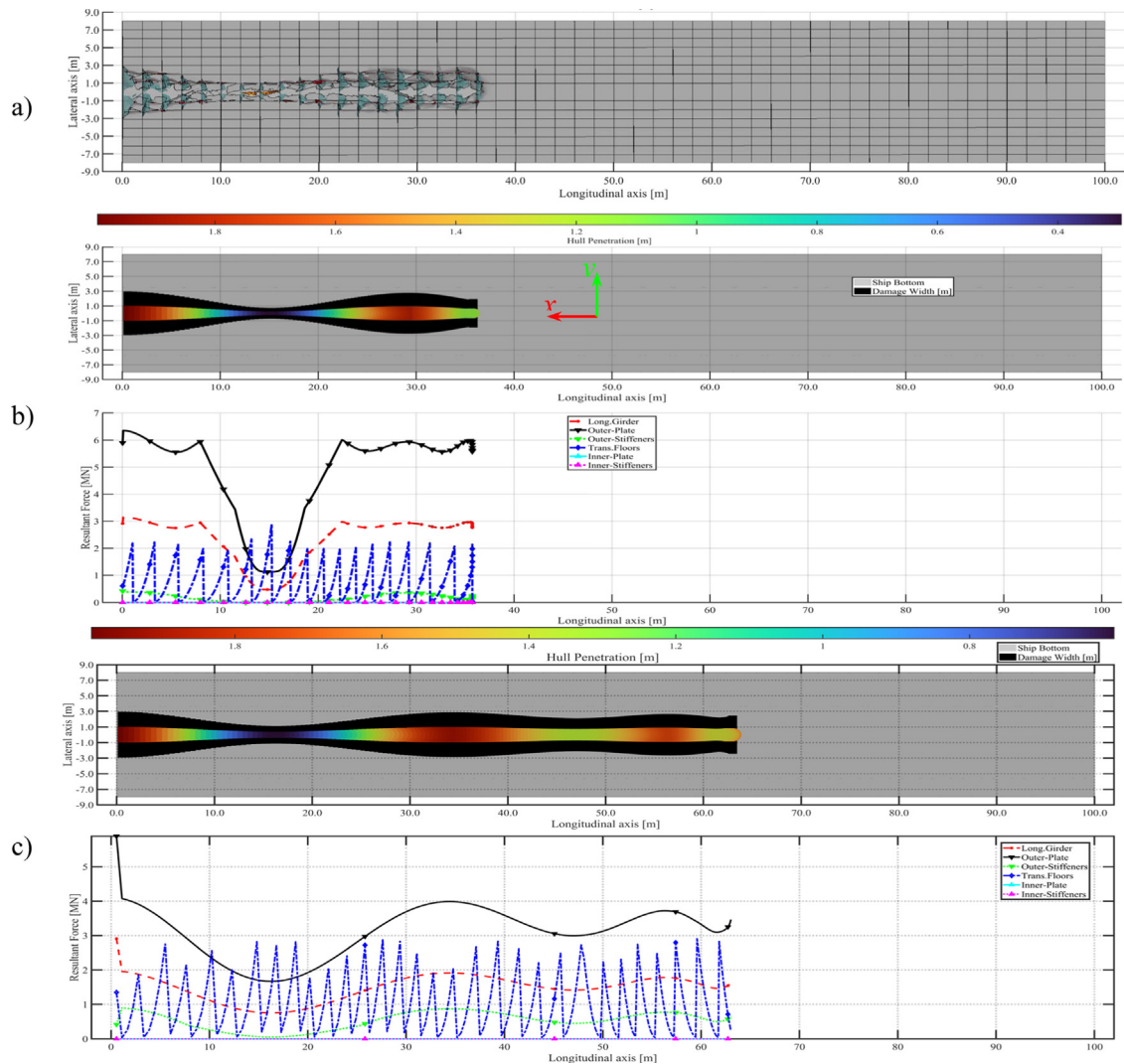


Fig. 16. Centerline box shape ship grounding damage profile from (a) LS-DYNA simulations; (b) present method; (c) Simonsen's method (1997a).

4.3. Numerical validation of a box-shaped ship subject to off-center (B/4) grounding

The results of the off-center grounding (quarter breadth of the ship B/4) are shown in Figs. 17–19. The total damage length of the ship predicted by the simplified FSI model is 49.7 m. This overestimates the LS-DYNA predictions by 4.7%. The trends of the surge, heave and pitch motions are similar for both models. During off-center grounding alongside heave and pitch, the ship also experiences roll motion. For the box-like idealization presented here, the simplified FSI model predicts a maximum roll velocity of 3.5 deg/s and heeling angle of the order of 9 deg. The latter exceeds almost 1.25 times predictions by LS-DYNA. The average longitudinal, lateral and vertical sliding force variations predicted by the simplified model differ by 7.8%, 10.0%, and 11.2% respectively to those predicted by LS-DYNA. The increased sway motion

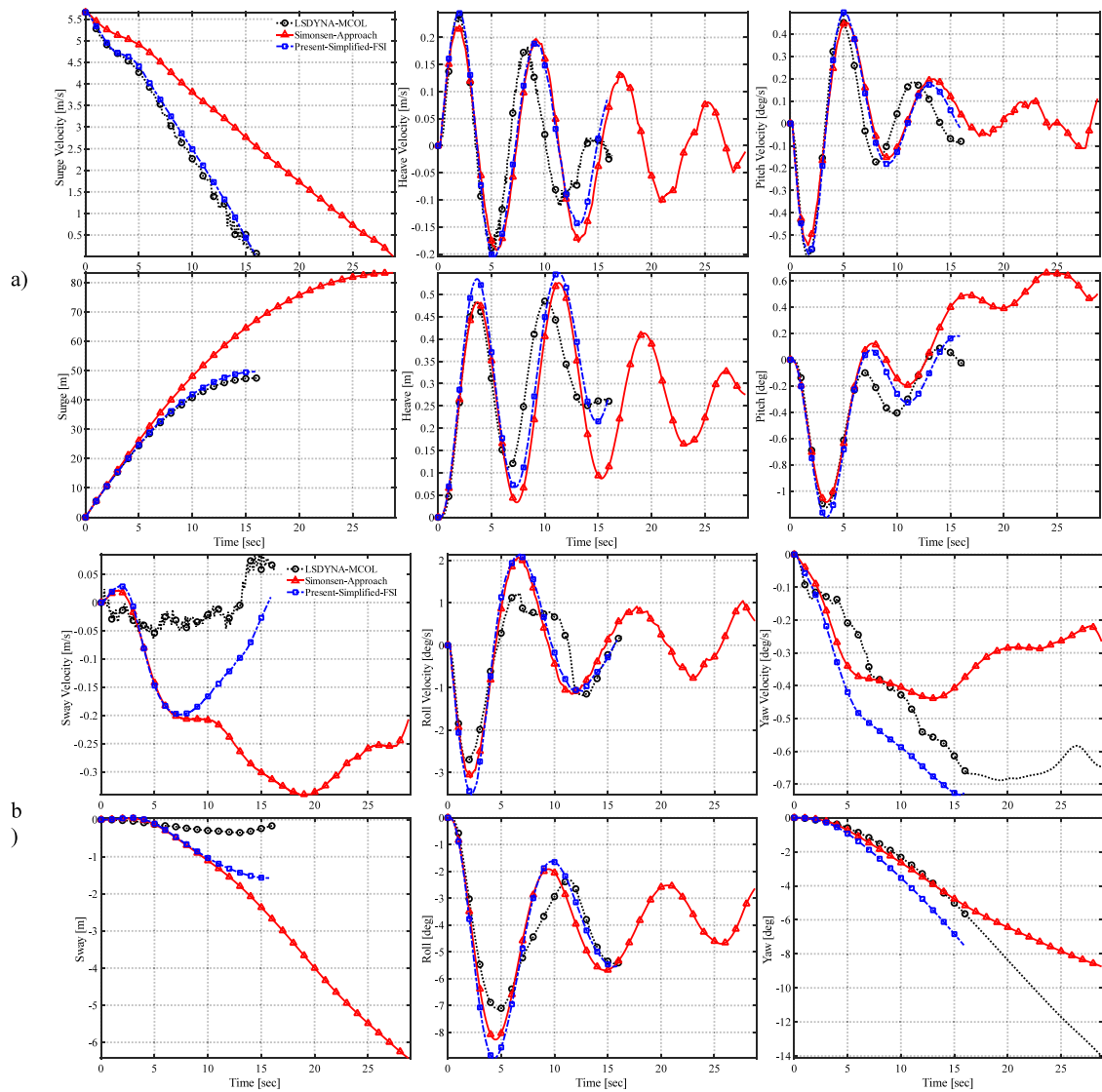


Fig. 17. Motions of off-center grounding (B/4) of a box shape ship. Velocities and displacements. (a) Surge, heave and pitch motion and (b) Sway, roll and yaw motion.

in the simplified model is predominantly caused by the large yaw and somewhat influenced by the roll inclination. The maximum total energy and sliding energy differences lie within 0.5% and 10% to those predicted by LS-DYNA.

A graphical illustration of damage extents from LS-DYNA simulations against Simonsen and the new model are shown in Fig. 19. Table 4 summarizes the differences in damage extents. The simplified model shows that in the transverse direction the damage reaches the centerline longitudinal girder, as the sway displacement increases by 0.5 m after 7 s. This becomes visible from the extent of the damage width in way of 31 m length of the damage (see Fig. 19). An off-center grounding demonstrates a similar tendency when a constant plate tearing angle (i.e., Simonsen's approach) is used. That is the substantial increase in damage extent may relate to a decrease in the total deformation energy (see Figs. 18, 19(c)). Irrespective of the model used noticeably the inner bottom remains intact because the height of the inner bottom is 2 m and the maximum penetration does not sufficiently exceed to rupture the inner plate. It is believed that some discrepancies may also arise because the non-linear Coriolis and centripetal forces due to added inertia as well as the history of motions and associated radiation damping forces are neglected in the simplified FSI model. Such effects may lead to a slight increase in the time-period of the heave and pitch motions (see Figs. 14 and 17(a)) as demonstrated by LS-DYNA simulations. In any case, the grounding dynamics of centerline and off-center grounding events compares well with the hydrodynamic damping, restoring forces, damage extents, deformation energy and contact forces (see Figs. 14–19).

A shortcoming of the proposed method is the accurate estimation of the lateral forces. This is based on the relative velocity between the ship and the rock used in the simplified FSI model (see Eq. (13)). LS-DYNA simulations demonstrate

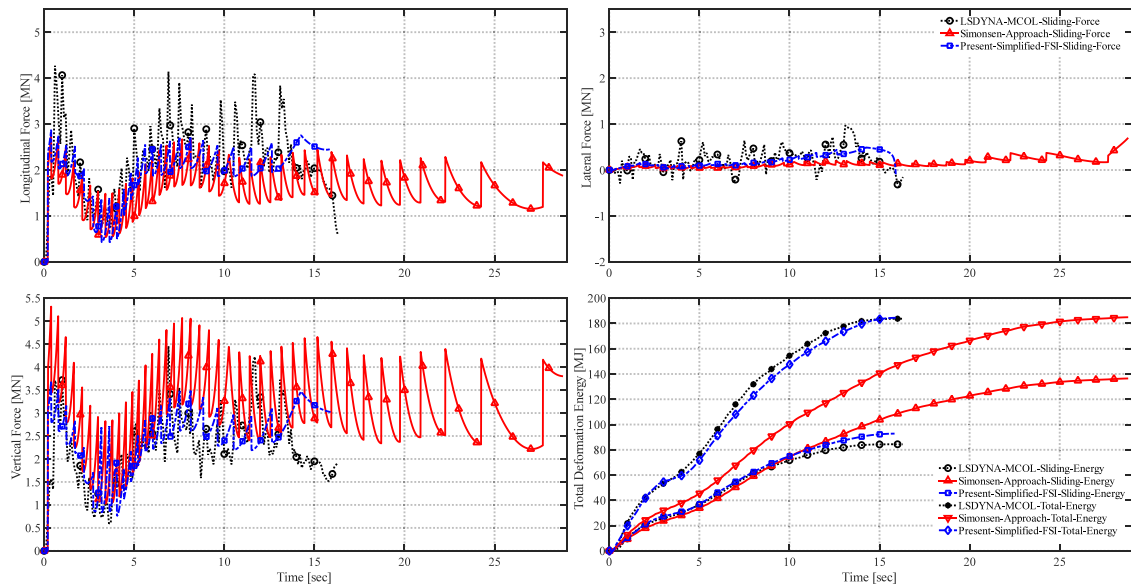


Fig. 18. Sliding forces and deformation energy of off-center grounding of box shape ship.

Table 4

Damage extents of the Off-center box-shape ship grounding. Comparison of the present model with LS-DYNA simulations.

	LSDYNA	Present model	% difference	Simonsen approach	% difference
Longitudinal extent (m)	47.5	49.7	4.63	81.09	70.7
Maximum width (m)	5.75	5.9	2.6	5.89	2.4
Minimum width (m)	1.9	1.35	29.0	1.77	6.8
Maximum penetration (m)	2.0	2.0	0	1.99	0.75
Minimum penetration (m)	0.28	0.26	7.1	0.42	50
Inner bottom breach	No	No	–	No	–

that lateral force discrepancy may emerge from the longitudinal member of the hull bottom. In an off-center grounding of the box-shape ship, the longitudinal stiffeners close to the base of the rock experience transverse deformation (see supplementary videos of box shape ship and Fig. 19a). However, the present model of Simonsen (1997a) does not consider the transverse deformation of the longitudinal members; as a result, the ship approaches the centerline girder due to increased rolling and yawing motion as the longitudinal stiffeners are unable to provide sufficient transverse resistance (see the deformation of longitudinal girder in a resistance force plot in Fig. 19(b)). As a result, the path of damage is more straight in LS-DYNA simulation in comparison to the simplified model (see Fig. 19).

4.4. Numerical validation of a passenger ship centerline grounding

The bottom structure details and hull profile of the FLOODSTAND SHIP B (Luhman et al., 2019) vary along the length of the ship. Structural particulars are illustrated in Fig. 13. The results of the centerline grounding simulation are shown in Figs. 20–22. The total length of the damage estimated by the rapid FSI model was 82.6 m. This is 20% lower than the one predicted by LS-DYNA (see Fig. 20) while differences are also evident in heave and pitch motions that associate with the forces leading to structural deformation. For example, the vertical force predicted by the simplified method has significantly higher values during the first 9 s of the simulation (see Fig. 21). The inconsistency in vertical force arises from the distinct shape of the bow and fore shoulder regions of the ship. The differences (see Fig. 22), may be attributed to the fact that the simplified FSI model accounts for a simplified tearing mode for the dynamics of the flat bottom plate (Simonsen, 1997a). In reality, the bow and forward end regions are not flat. This results in a larger gap opening of the bow region and an overestimation of plate resistance and girder forces (see Appendices B and C). Vertical forces influenced by complex geometries are not accounted for by the simplified FSI approach. The mean deviation of the horizontal force is less than 0.5%. The average difference of vertical forces between the simplified FSI model and LS-DYNA simulation is approximately 28.5%. The total sliding energy from the rapid FSI model is marginally higher around 5.2%. On the contrary, the total deformation energy is almost 12.5% lower as compared to LS-DYNA results (see Fig. 21).

Table 5 and Fig. 22, display a comparison between the damage extents predicted by LS-DYNA simulations, the simplified FSI model and the Simonsen approach for the case of centerline grounding. The longitudinal location (position) of maximum damage width obtained using the simplified model and LS-DYNA simulation are at 4.5 m and at 103 m from

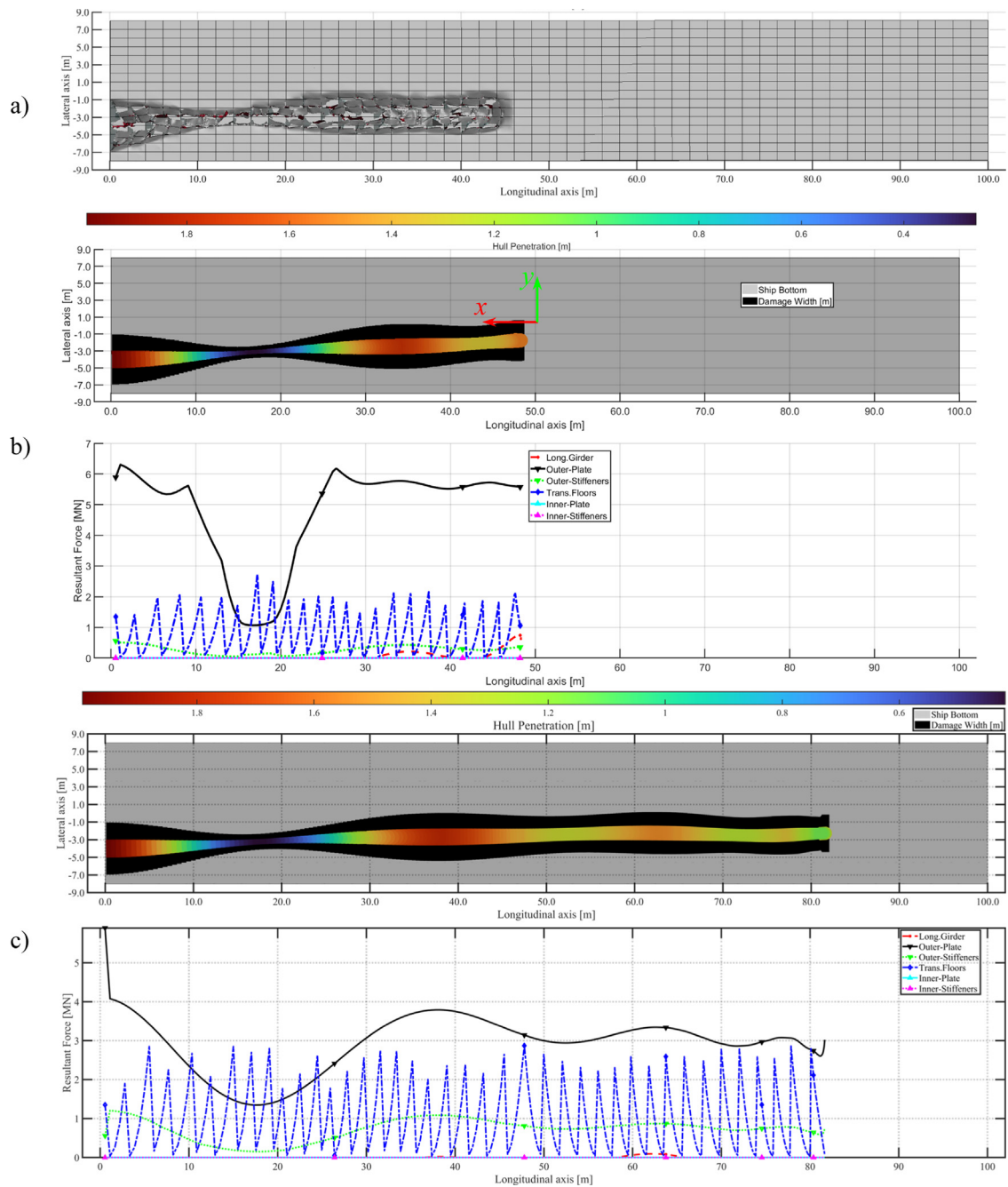


Fig. 19. Off-center box shape ship grounding damage profile resulting from (a) LSDYNA simulations; (b) new model and (c) Simonsen's method (1997a).

the bulbous bow tip, respectively (see encircled region in Fig. 22). This deviation is due to the complex bow geometry of the ship where the simplified model overpredicts the deformation width. This is not the case for the box shape ship (see Sections 4.2 and 4.3) where maximum and minimum damage widths obtained from the simplified FSI model and LS-DYNA simulations almost coincide.

The double bottom configuration along the length of the passenger ship varies. From the tip of the bulbous bow to a distance of 43 m towards the aft of the ship, the height of the double bottom is greater than 2.5 m. After 43 m from the bow tip, the double bottom height reduces to 1.6 m (see Fig. 13). The variations of resultant deformation forces for plates, girders, stiffeners, and floors are demonstrated in Fig. 22 and the supplementary material submitted for the case of passenger ship grounding. The simplified FSI model illustrates good quality results as it reasonably captures the forces

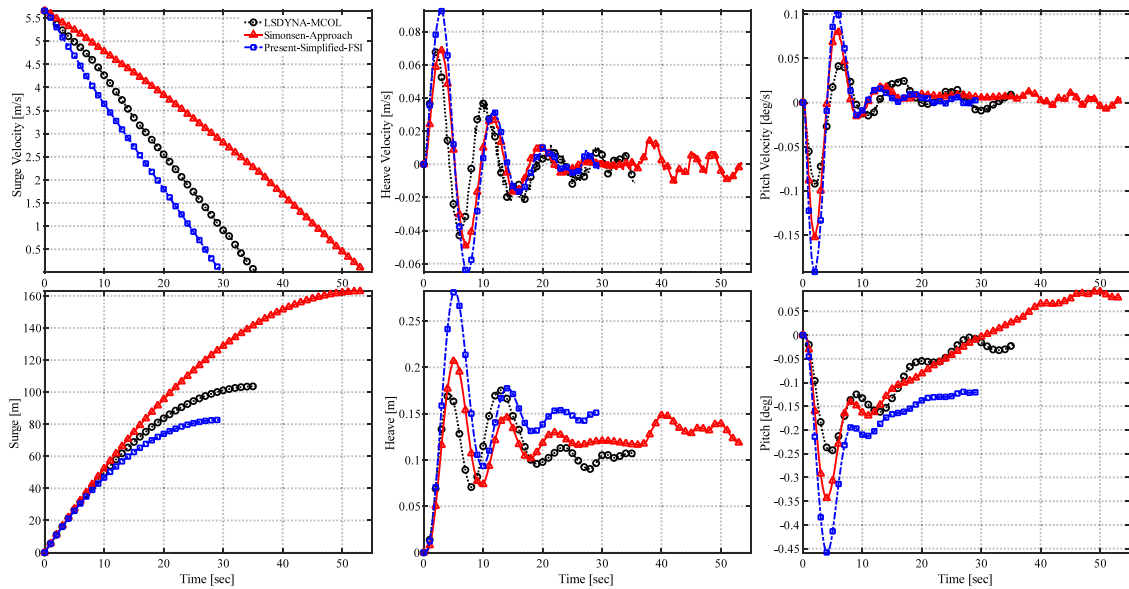


Fig. 20. Motions of centerline grounding of a passenger ship. Top velocities and bottom displacements.

Table 5

Centerline passenger ship grounding. Comparison of the present model with LS-DYNA simulations.

	LSDYNA	Present model	% difference	Simonsen approach	% difference
Longitudinal extent (m)	103.5	82.6	20	161.22	55.7
Maximum width (m)	5.8	5.34	8	5.6	3.45
Minimum width (m)	2.33	1.89	18.9	1.89	18.88
Maximum penetration (m)	1.89	1.78	5.8	1.88	0.52
Minimum penetration (m)	1.32	0.85	39.5	0.46	65.15
Inner bottom breach	Yes	Yes	–	Yes	–

of the structural components. Moreover, as the position of the ship center of gravity reaches closer to the rock the pitch motion reaches zero (see Fig. 20). Once again, Simonsen's approach overestimates the damage length. As the damage length reaches approximately 145 m, the rock interacts with the girders (see Fig. 13). This increases the girder force as seen in Fig. 22c.

4.5. Numerical validation of a passenger ship off-center (B/4) grounding

Results for the case corresponding to off-center (B/4) grounding of a passenger vessel are shown in Figs. 23–26. The results of the surge, heave, and pitch motions match well. The total damage length of the ship when using the simplified FSI model is almost equal to LS-DYNA simulation. Comparison of the surge velocities from LS-DYNA simulation and present model shows that the grounding event terminates after 30.6 s and 33.2 s respectively. A constant surge velocity is attained after 30 s (see Fig. 23). The difference in the surge velocity may be attributed to the lower estimation of the horizontal force by the simplified FSI model. The simplified FSI model shows on average 10% lower values of longitudinal resistance in comparison to LS-DYNA (see Fig. 24). On the other hand, the trends of vertical force estimates compare well. The variation of vertical force is also reflected in heave motions where the simplified FSI model has slightly less heave amplitude.

The differences in the roll response between LS-DYNA and the simplified model are significant. LS-DYNA simulations show that when the rock is in between two longitudinal girders, roll motion is steadily increasing but is delayed in comparison to the values predicted by the simplified FSI model (see supplementary videos of passenger ship off-center grounding). During the first 6.7 s of the LS-DYNA simulation, the centerline longitudinal hull girder (Girder-1) is in contact with the rock (see Fig. 25). Transverse forces from Girder-1 subsequently incline the ship towards Girder-2, which is located nearly at the extreme width of the ship (see supplementary videos of passenger ship off-center grounding, Figs. 24 and 25). However, after 6.7 s the rock conforms to Girder-2 which bends. This ultimately affects ship sway and yaw motions (see Fig. 23). The trend of the sway directional lateral force predicted by the simplified FSI model is different from that of LS-DYNA. The differences in average forces predicted by both models are within the acceptable numerical error (just 2%). However, the differences in total deformation and sliding energy predicted by the simplified FSI and LS-DYNA models 10% and 4% respectively (see Fig. 24).

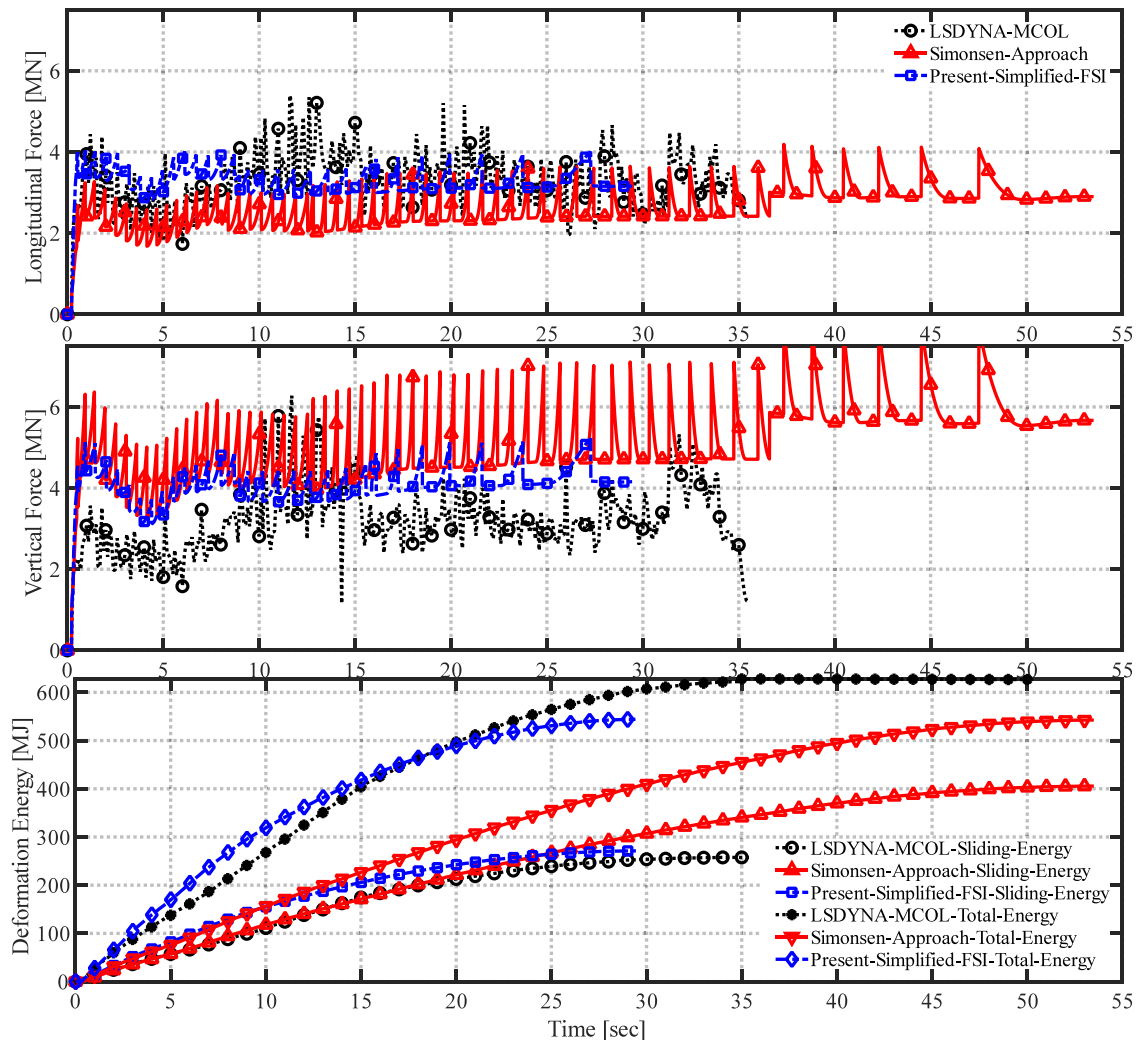


Fig. 21. Sliding forces and deformation energy of centerline grounding of a passenger ship.

The details of damage extents for the case of the passenger ship off-center grounding are shown in Table 6. The maximum deformation width and hull penetration estimated by the simplified FSI model are lower in comparison to those from LS-DYNA. Notwithstanding this, the differences in the maximum extent of damage is within 10% of LS-DYNA simulations. In both cases, the inner bottom ruptures (see Fig. 26). For off-center grounding when the ship rolls the location of the rock gets closer to the centerline and the longitudinal girders in between the rock tip and centerline girder may deform (see Fig. 26 after 94 m of the ship's length). Overall, the Simonsen technique underestimates total deformation energy and forces, resulting in an increase in damage length and the inability to approximate the real scenario. Table 7, summarizes the comparison of the computation time of the present simplified FSI model against LS-DYNA simulations. LS-DYNA simulations were performed using parallel execution with 120 parallel processing (MPP) processors. Table 7, shows that the simplified FSI model drastically reduces the computational effort in comparison to the fully coupled FSI model of LS-DYNA and can be used for stochastic assessment of ship damage extents.

5. Conclusions

This paper proposed a rapid FSI method for the realistic assessment of ship grounding dynamics. The model is validated by direct comparisons against LS-DYNA-MCOL and the simplified crashworthiness model of Simonsen (1997a) for the case of a barge and a modern cruise vessel. The new rapid assessment model provides more realistic results in comparison to the method of Simonsen (1997a) that assumes constant plate split angle and therefore overestimates ship damage extents. Comparisons against LS-DYNA-MCOL simulations show good agreement in terms of longitudinal and vertical

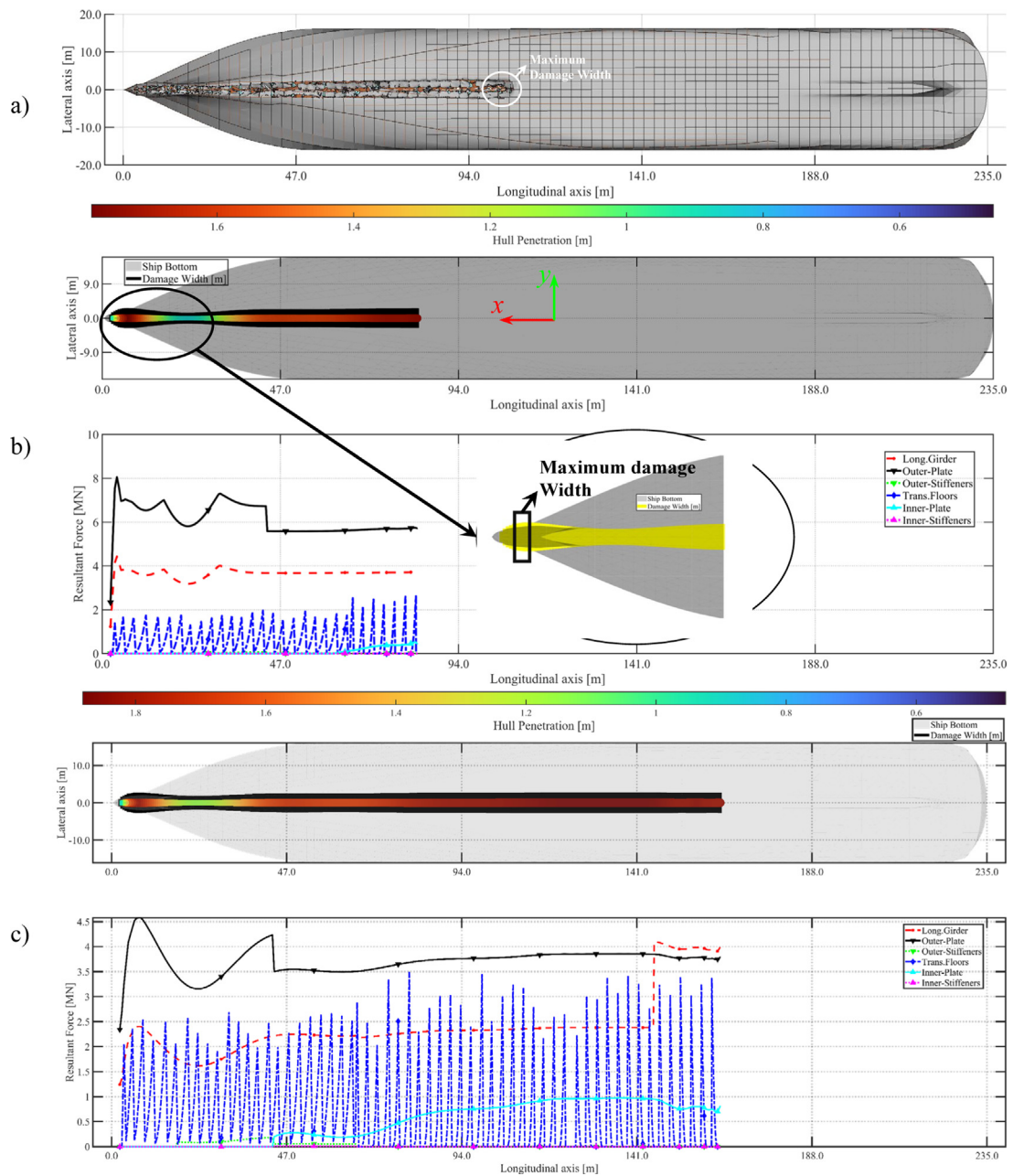


Fig. 22. Centerline passenger ship grounding damage profile from (a) LS-DYNA simulations; (b) new model and (c) Simonsen's approach (1997a).

Table 6

Damage extents of the Off-center passenger ship grounding. Comparison of the present model with LS-DYNA simulations.

	LSDYNA	Present model	% difference	Simonsen approach	% difference
Longitudinal extent (m)	119.13	119.8	0.56	121.0	1.56
Maximum width (m)	5.3	5.08	4.2	5.11	3.5
Minimum width (m)	1.7	1.3	23.5	1.74	2.35
Maximum penetration (m)	1.86	1.68	9.7	1.69	9.13
Minimum penetration (m)	0.36	0.24	7.1	0.04	88.8
Inner bottom breach	Yes	Yes	-	Yes	-

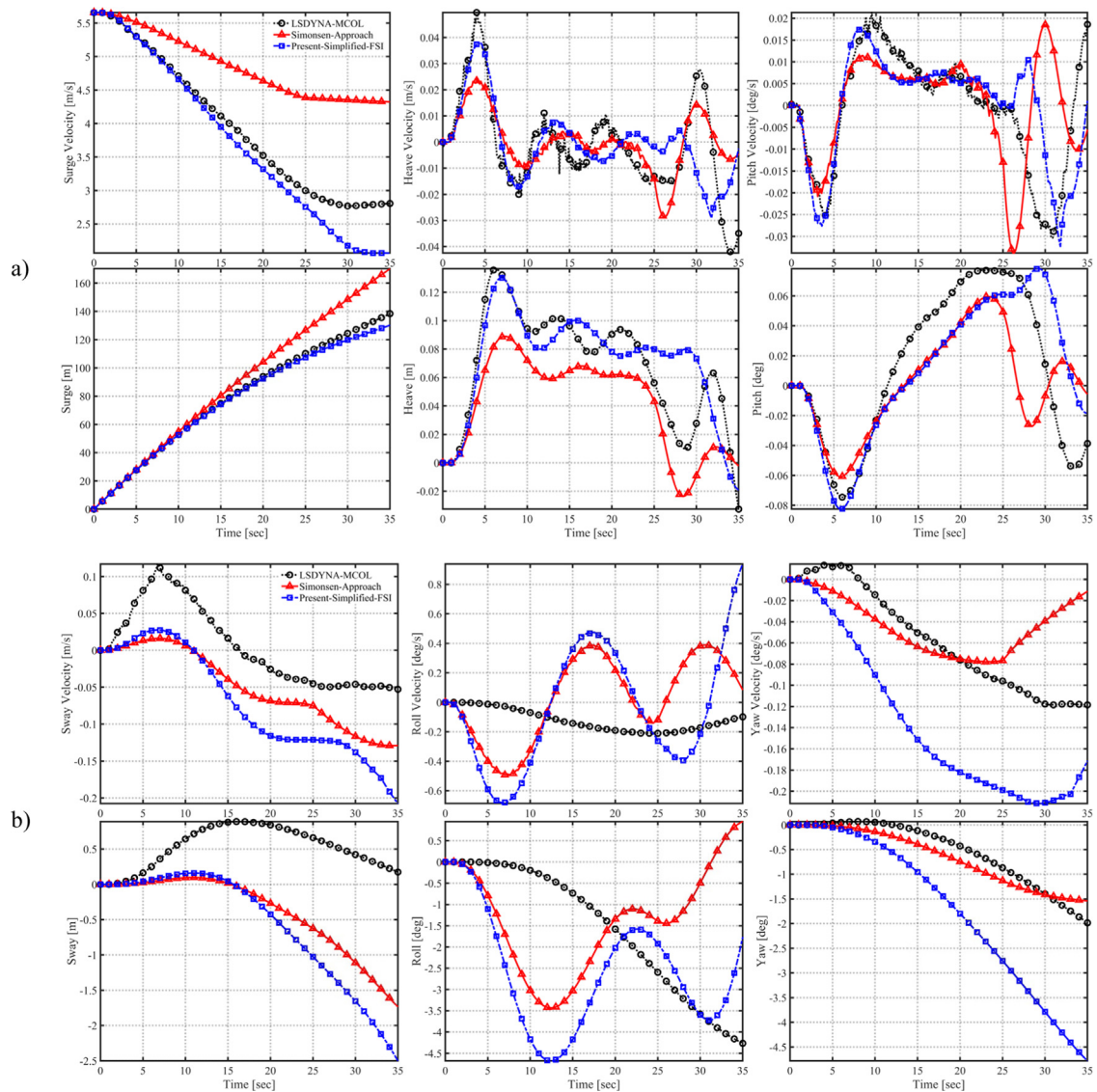


Fig. 23. Motions of side (B/4) grounding of a passenger ship. Velocities and displacements. (a) Surge, heave and pitch motions and (b) Sway, roll and yaw motions.

Table 7

Comparison of simulation time from simplified model and LS-DYNA simulations, for a box and passenger vessel.

	Box-shape ship				Passenger ship			
	Simplified FSI		LSDYNA		Simplified FSI		LSDYNA	
	Center	Off-center	Center	Off-center	Center	Off-center	Center	Off-center
Simulation time (s)	50	50	50	50	50	50	50	50
CPU time (s)	0.64	0.61	13628	16503	0.63	0.58	37061	30778
CPU time (hh:mm:ss)	00:00:01	00:00:01	03:47:08	04:35:03	00:00:01	00:00:01	10:17:41	08:32:58

forces, damage length, width, hull penetration and deformation energy. However, for the cruise ship study case, the lateral forces are to some extent underestimated. This could be attributed to the fact that the rapid FSI model does not account for the influence of lateral loading on the longitudinal members of complex geometries in way of the extremities of the

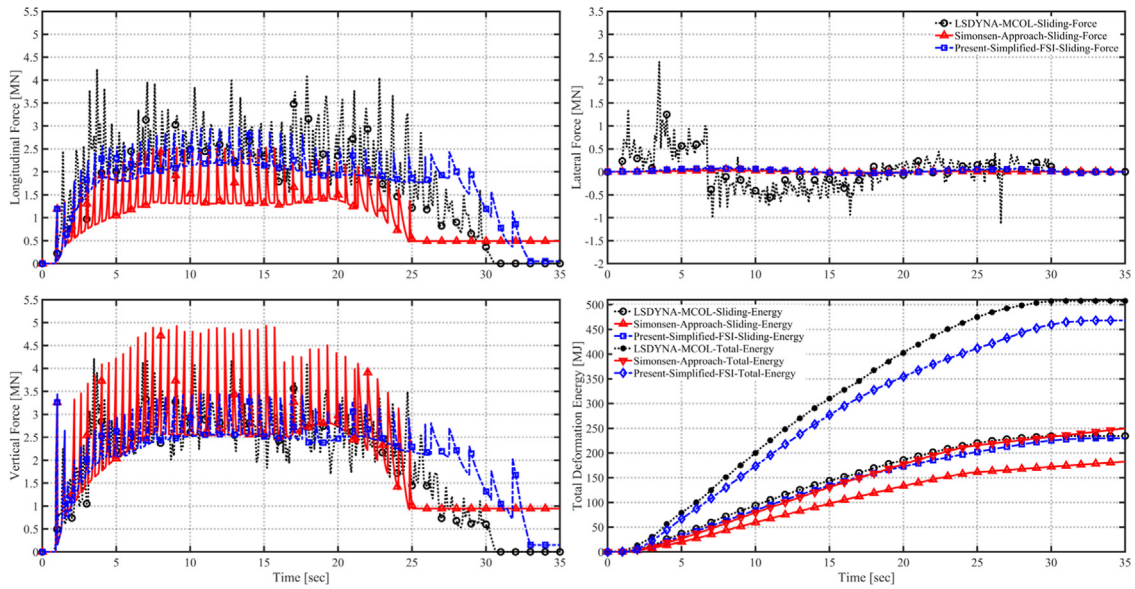


Fig. 24. Sliding forces and deformation energy of side (B/4) grounding of a passenger ship.

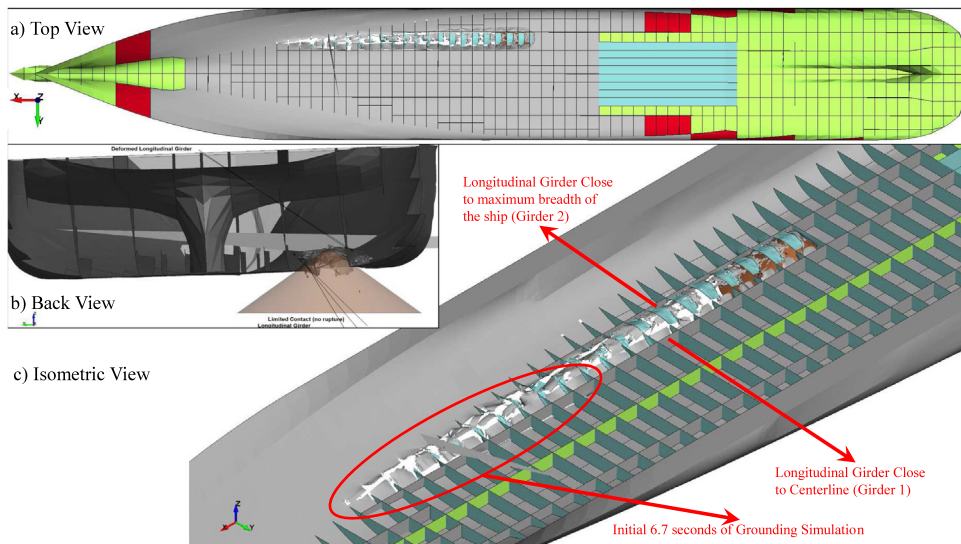


Fig. 25. Off-center grounding LSDYNA-MCOL validation study, rock locked in between two longitudinal girders.

hull (e.g., hull curvatures towards ship bow). To resolve this discrepancy future research could focus on the development of an analytical formulation that accounts for transverse deformation of longitudinal members and tearing of the bow region of the ship. Notwithstanding this, the method may be considered significantly advanced in comparison to simplistic models and empirical data sets used by existing damage stability regulations. It also accounts for the influence of evasive maneuvers on the response (Conti et al., 2021). In this sense it could also serve as useful update in algorithms used by modern navigation decision support systems (Gil et al., 2020; Zhang et al., 2021, 2022).

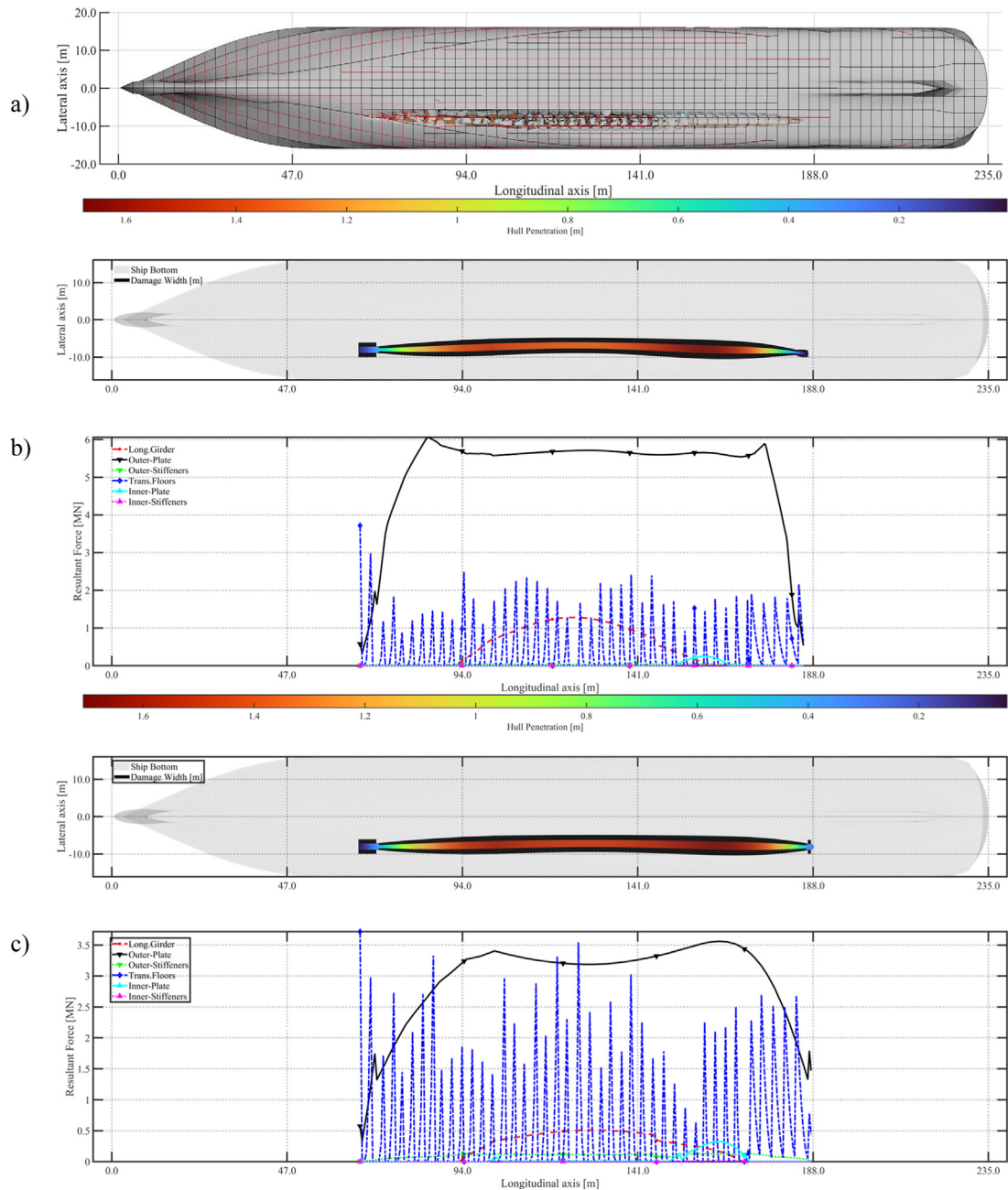


Fig. 26. Off-centerline (B/4) passenger ship grounding damage profile (a) LS-DYNA simulations; (b) new model and (c) Simonsen's approach (1997a).

CRedit authorship contribution statement

Ghalib Taimuri: Methodology, Contact algorithm software development and validation, Formal analysis, Investigation, Data curation, Writing – original draft, Writing – review & editing. **Sang Jin Kim:** Software, Review, Investigation. **Tommi Mikkola:** Methodology, Review, Supervision. **Spyros Hirdaris:** Conceptualization, Methodology, Review & editing, Supervision, Resources, Funding acquisition.

Declaration of competing interest

The authors declare that they have no known competing financial interests or personal relationships that could have appeared to influence the work reported in this paper.

Acknowledgment

The authors thank Prof. Hervé Le Sourne (ICAM, Nantes, France) for his useful advise on LS-DYNA–MCOL coupling methods and acknowledge CSC – IT Center for Science, Finland, for the provision of generous computational resources used for the 3D simulations presented in this paper. Funding received from EU Horizon 2020 project FLooding Accident REsponse (FLARE – Contract No. 814753) is greatly acknowledged.

Appendix A

Rigid body ship kinetics

According to Fossen (2011) and Lewandowski (2004) for the case of a symmetric displacement monohull the inertia and added inertia matrices are expressed as:

$$\mathbf{M} = \begin{bmatrix} m & 0 & 0 & 0 & mz_G & 0 \\ 0 & m & 0 & -mz_G & 0 & mx_G \\ 0 & 0 & m & 0 & -mx_G & 0 \\ 0 & -mz_G & 0 & I_x & 0 & -mx_G z_G \\ mz_G & 0 & -mx_G & 0 & I_y & 0 \\ 0 & mx_G & 0 & -mx_G z_G & 0 & I_z \end{bmatrix} \quad (16)$$

$$\mathbf{M}_A = \begin{bmatrix} -X_{\dot{u}} & 0 & 0 & 0 & -0.5X_{\dot{u}}T & 0 \\ 0 & -Y_{\dot{v}} & 0 & -Y_{\dot{p}} & 0 & -Y_{\dot{r}} \\ 0 & 0 & -Z_{\dot{w}} & 0 & -Z_{\dot{q}} & 0 \\ 0 & -K_{\dot{v}} & 0 & -K_{\dot{p}} & 0 & -K_{\dot{r}} \\ -0.5X_{\dot{u}}T & 0 & -Z_{\dot{q}} & 0 & -M_{\dot{q}} & 0 \\ 0 & -N_{\dot{v}} & 0 & -K_{\dot{r}} & 0 & -N_{\dot{r}} \end{bmatrix} \quad (17)$$

where, m is the mass of the ship; I_x , I_y and I_z are the moments of inertia of the ship around the x , y , and z -axes. In this paper the added mass coefficients in \mathbf{M}_A were obtained from linear strip theory. In the method proposed in this paper, the influence of time variation of added mass in way of contact was ignored and therefore the encounter frequency was assumed to be infinite during grounding contact. The mass multiplier terms in a rigid body inertia matrix (\mathbf{M}) arise because the origin is located at a distance \bar{r}_G away from CoG. For the same reason, Coriolis and centripetal forces also include the effect of origin shift so that:

$$\mathbf{C} = \begin{bmatrix} 0 & 0 & 0 & mz_G r & -mx_G q + mw & -mx_G r - mv \\ 0 & 0 & 0 & -mw & mz_G r + mx_G p & mu \\ 0 & 0 & 0 & -mz_G p + mv & -mz_G q - mu & mx_G p \\ -mz_G r & mw & mz_G p - mv & 0 & -mx_G z_G p + I_z r & -I_y q \\ mx_G q - mw & -mz_G r - mx_G p & mz_G q + mu & mx_G z_G p - I_z r & 0 & -mx_G z_G r + I_x p \\ mx_G r + mv & mu & -mx_G p & I_y q & mx_G z_G r - I_x p & 0 \end{bmatrix} \quad (18)$$

Only small out-of-plane motions were considered. This means any changes in the waterplane area were independent of heave, roll, and pitch motions. The restoring force matrix given in Eq. (19) shows the combination of the effect of ship weight and buoyancy.

$$\mathbf{K} = \begin{bmatrix} 0 & 0 & 0 & 0 & -\rho g A_{WP} \Delta z & 0 \\ 0 & 0 & 0 & \rho g A_{WP} \Delta z \cos(\theta) & 0 & 0 \\ 0 & 0 & \rho g A_{WP} \cos(\phi) \cos(\theta) & 0 & \rho g A_{WP} x_f & 0 \\ 0 & 0 & 0 & mg GM_{T0} \cos(\phi) \cos(\theta) & 0 & 0 \\ 0 & 0 & \rho g A_{WP} x_f & 0 & mg GM_{L0} \cos(\phi) \cos(\theta) & 0 \\ 0 & 0 & 0 & \rho g \nabla GM_{T0} \sin(\theta) & -\rho g \nabla GM_{L0} \cos(\theta) \sin(\phi) & 0 \end{bmatrix} \quad (19)$$

The damping ratios ζ_w , ζ_ϕ and ζ_θ were evaluated numerically from the nonlinear time-domain 6-DoF potential flow solver of Matusiak (2021) following a numerical decay test. The validation of external ship dynamics is presented in Taimuri et al. (2020).

As part of the numerical decay test, the ship was assumed to progress in calm seas along a straight line with different initial velocities. She was released from an initial heave displacement, and initial roll and pitch inclination. The resulting heave, roll and pitch motions were measured separately to compute the damping ratio ζ , from the successive maxima

(R_n and R_{n+1}) of the decaying motion given in Eq. (20).

$$\begin{aligned}\zeta_{w,\phi,\theta} &= \frac{1}{2\pi} \ln \left(\frac{R_n}{R_{n+1}} \right), \\ \omega_w &= \sqrt{\frac{\rho g A_{wp}}{m - Z_{\dot{w}}}}, \\ \omega_\phi &= \sqrt{\frac{mgGM_{T0}}{I_x - K_{\dot{\phi}}}}, \\ \omega_\theta &= \sqrt{\frac{mgGM_{L0}}{I_y - M_{\dot{\theta}}}}\end{aligned}\quad (20)$$

Damping forces were then evaluated from the natural (heaving, rolling and pitch) frequency of the ship as presented in Eqs. (21) and (22). The curve fits were performed on the damping ratios (ζ_w, ζ_ϕ , and ζ_θ ; Fig. 27) as a function of the Froude number. These values of damping ratios are used in a time-domain maneuvering simulation to evaluate radiation damping of the ship Eq. (21). The plots of decaying inclination (roll and pitch) and displacement (heave), and curve fitted damping ratios are illustrated in Fig. 27. The hydrodynamic damping coefficients \mathbf{B}_H were assumed coupled only for in-plane (surge, sway, and yaw) motions (Taimuri et al., 2019). Heave, pitch, and roll damping effects expressed by the term \mathbf{B}_p accounted for wave radiation effects.

$$\mathbf{B}_p = \begin{bmatrix} 0 & 0 & 0 & 0 & 0 & 0 & 0 \\ 0 & 0 & 0 & 0 & 0 & 0 & 0 \\ 0 & 0 & 0 & 2\zeta_w\omega_w & 0 & 0 & 0 \\ 0 & 0 & 0 & 0 & 2\zeta_\phi\omega_\phi & 0 & 0 \\ 0 & 0 & 0 & 0 & 0 & 2\zeta_\theta\omega_\theta & 0 \\ 0 & 0 & 0 & 0 & 0 & 0 & 0 \end{bmatrix} [M + M_A] \quad (21)$$

$$\begin{aligned}\mathbf{B}_H &= \frac{1}{2} \rho \cdot L (u^2 + v^2) \\ &\times \begin{bmatrix} 0 & X_{vv}v + X_{vvv}v^3 & 0 & 0 & 0 & X_{vr}v + X_{rr}r \\ 0 & Y_v + Y_{vv}v + Y_{vvv}v^2 + Y_{vvr}vr & 0 & 0 & 0 & Y_r + Y_{rr}r + Y_{rrr}r^2 + Y_{vrr}vr \\ 0 & 0 & 0 & 0 & 0 & 0 \\ 0 & 0 & 0 & -0.5TY_{hull} & 0 & 0 \\ 0 & 0 & 0 & 0 & 0 & 0 \\ 0 & (N_v + N_{vv}v + N_{vvv}v^2 + N_{vvr}vr)L & 0 & 0 & 0 & (N_r + N_{rr}r + N_{rrr}r^2 + N_{vrr}vr)L \end{bmatrix}\end{aligned}\quad (22)$$

Appendix B

Membrane straining of plate (Simonsen, 1997a)

The membrane strain of the plate is illustrated in Fig. 4, which is defined as:

$$\begin{aligned}u_0 &= B_{de} \sqrt{(1 - \cos \alpha)^2 \sin^2 \theta + (1 - \cos \theta)^2 \sin^2 \alpha} \\ v_0 &= B_{de} \left(\frac{1}{\cos \alpha} - 1 \right)\end{aligned}\quad (23)$$

where v_0 is half the length of the maximum transverse opening; u_0 is the longitudinal gap opening of the plate.; θ is the plate split angle; B_{de} represents the deformation width and α is the flap angle representing the formation of the hinge line.

Description of the mechanics of transverse damage extents (Simonsen, 1997a)

During ship grounding the stiffeners along the longitudinal direction of the bottom plate structure will deform. In addition, because of the influence of membrane stresses and transverse floor deflections deformation effects will extend to the nearest longitudinal. The critical distance of this longitudinal from the rock is defined as:

$$s_{l,c} = R_R \sqrt{1 - e^{-2\epsilon_{cr}}}\quad (24)$$

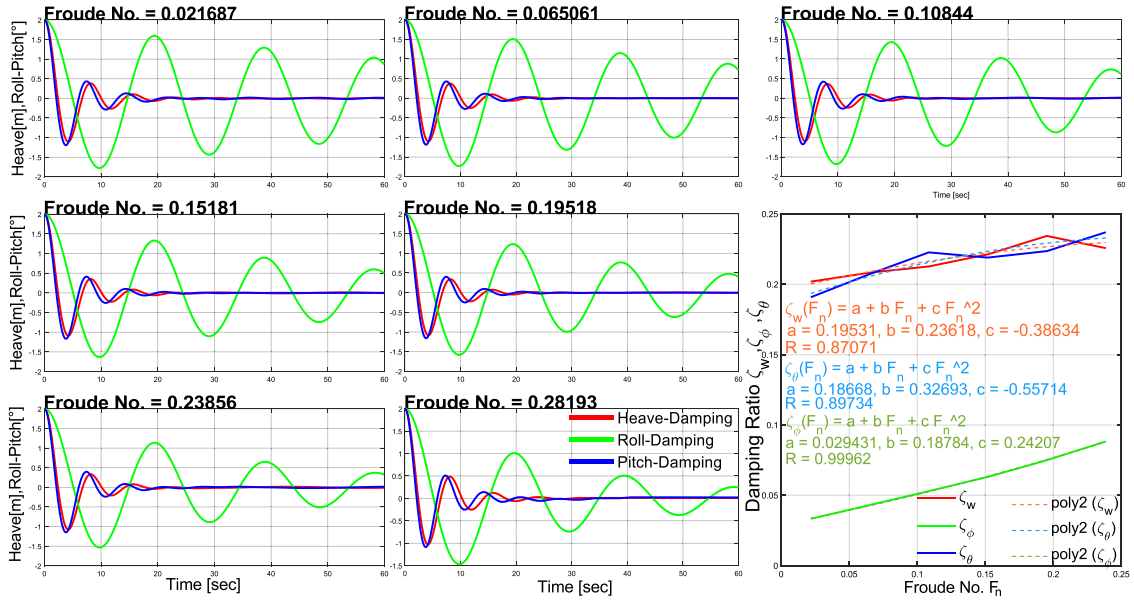


Fig. 27. Demonstration of results from the numerical decay test used to estimate heave, roll and pitch damping ratios. Froude numbers are shown on top of each subplot. The last (bottom right) plot represents the curve fitting of the damping ratio as a function of Froude number.

where R_R is the rounded tip radius of the cone representing the rock tip (Fig. 3); ϵ_{cr} is the critical rupture strain of the material. Consequently, the penetration due to fracture is defined as:

$$\delta_{fra} = R_R \left\{ 1 - \cos \psi_C + \sin^2 \psi_C \ln \left[\frac{\frac{s_{lf}}{R_R} + \sqrt{\left(\frac{s_{lf}}{R_R}\right)^2 - \sin^4 \psi_C}}{\sin \psi_C (1 + \cos \psi_C)} \right] \right\} \quad (25)$$

$$\psi_C = \cos^{-1} (e^{-\epsilon_{cr}})$$

where, δ_{fra} is the critical penetration causing the plate to rupture; s_{lf} is the lateral extent of deformation from rock tip to the first longitudinal stiffener outside $s_{l,c}$ and ψ_C is the plate wrapping angle on the rock.

The extent of the transverse deformation before fracture (intact condition) and the width of the damage in case of fracture were defined as:

$$B_{de} = s_{lf} \text{ for } \delta_{out} < \delta_{fra}, \text{ else}$$

$$B_{de} = \begin{cases} \sqrt{R_R^2 - (\delta_{out} - R_R)^2} & \text{for } \delta_{out} < R_R(1 - \sin \phi) \\ \tan \phi (\delta_{out} + R_R(1/\sin \phi - 1)) & \text{for } \delta_{out} \geq R_R(1 - \sin \phi) \end{cases} \quad (26)$$

where, δ_{out} is the penetration of the rock inside the hull. It is noted that the penetration into the hull δ_{out} originates from the contact detection approach (see Section 3.4).

Description of the mechanics of longitudinal damage extents (Sun et al., 2017)

Deformation initiates once the base of the rock is in contact with the floor bottom plate (see Fig. 28). The vertical height of the deformed floor H_{def} is defined as:

$$H_{def} = \frac{\Delta_t}{\tan \phi}, \text{ where} \quad (27)$$

$$\Delta_t = |\text{mod}(|x_{int} - B_{de}|, \chi_t) - \chi_t|$$

where Δ_t is the deflection of the transverse web floor; ϕ is the cone semi apex angle; χ_t is transverse floor spacing

During deformation the floor is longitudinally transfers from line AE to line ACF Fig. 28. Therefore the critical fracture strain of the deformed floor is defined as:

$$\epsilon_f = \frac{B_{de}\theta_t + \sqrt{b_{l,Gir}^2 + (\Delta_t - B_{de})^2 - B_{de}^2} - b_{l,Gir}}{b_{l,Gir}} \quad (28)$$

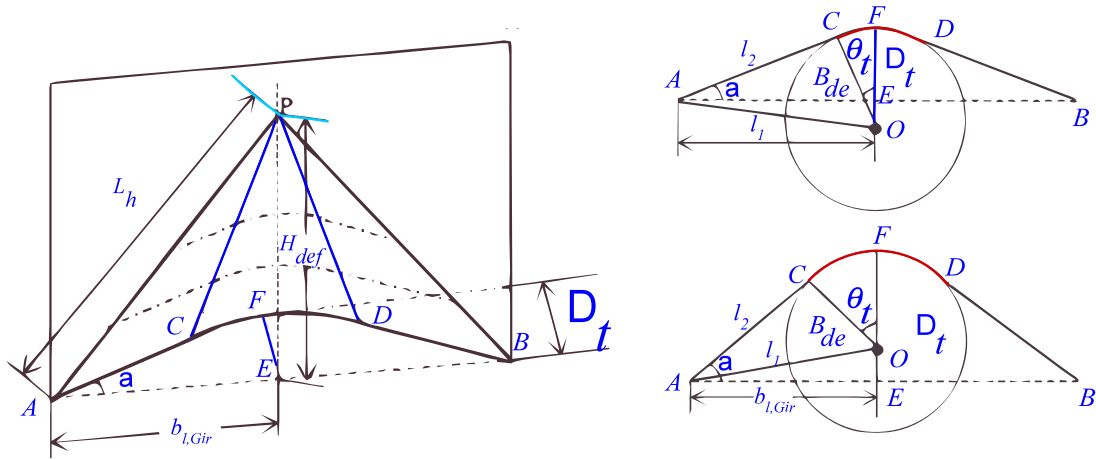


Fig. 28. The extent of the longitudinal direction, floor deformation (Sun et al., 2017).

where $b_{l,Gir}$ is half the spacing in between two longitudinal girders; θ_t is half of the arc CD Fig. 28, which is obtained from the geometry of the floor deformation as:

$$\theta_t = \begin{cases} \tan^{-1} \frac{b_{l,Gir}}{B_{de} - \Delta_t} - \cos^{-1} \frac{B_{de}}{\sqrt{b_{l,Gir}^2 + (\Delta_t - B_{de})^2}}, & \Delta_t < B_{de} \\ \pi - \tan^{-1} \frac{b_{l,Gir}}{\Delta_t - B_{de}} - \cos^{-1} \frac{B_{de}}{\sqrt{b_{l,Gir}^2 + (\Delta_t - B_{de})^2}}, & \Delta_t \geq B_{de} \end{cases} \quad (29)$$

The algorithm developed is illustrated in Fig. 29. The mechanics of intact and fractured plate conditions are specified in Eq. (25). The overall plate topology (i.e., unstiffened plate, girders, floors, and stiffeners) was assumed to remain in contact with the rock without fracture when the rock is adequately blunt (i.e., the penetration is lower than δ_{fra} or the cone apex angle $\phi > \phi_c$). The critical apex angle ϕ_c was defined according to Simonsen (1997a) as:

$$\phi_c = \sin^{-1} [e^{-\epsilon \sigma}] \quad (30)$$

Plastic resistance forces of structural members

According to the upper bound theorem of plasticity, the resistance forces were computed by assuming a mode that accounts for the effects in way of the crack tip, bending hinge line, and membrane deformation. Appendix C summarizes the plastic intact and fracture forces defined by Simonsen (1997a) and Sun et al. (2017).

Appendix C. Plastic resistance forces on structural member (Simonsen, 1997a; Sun et al., 2017)

M_0	$\frac{\sigma_0 t^2}{2\sqrt{3}}$, plastic bending moment
N_0	$\frac{2}{\sqrt{3}}\sigma_0 t$, plastic membrane force
F_{plate_i}	$2N_0 v_0 \left(\sqrt{1 + \frac{1}{4} \tan^2 \theta_p} + \frac{1}{2} \left(\frac{u_0}{v_0} + \tan \theta_p \right) \right) + 4M_0 \tan^{-1} \left(\frac{\delta_{out}}{S_{if}} \right) + 16M_0 \frac{S_{if}}{\delta_{out}} \ln \left[\left(\frac{\delta_{out}}{L_{de}} \right)^2 + 1 \right]$
	$\begin{cases} u_0 = S_{if} \sqrt{(1 - \cos \alpha)^2 \sin^2 \theta_p + (1 - \cos \theta_p)^2 \sin^2 \alpha} \\ v_0 = S_{if} \left(\frac{1}{\cos \alpha} - 1 \right); \alpha = \tan^{-1} \left(\frac{\delta_{out}}{S_{if}} \right); L_{de} = \frac{S_{if}}{\tan \theta_p} \end{cases}$

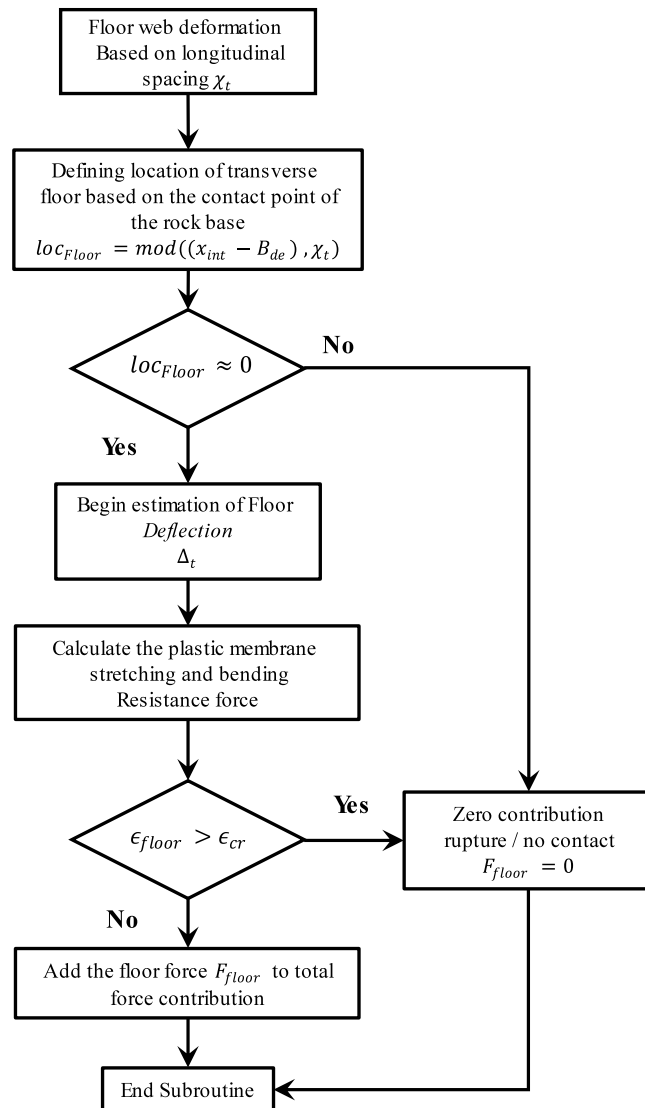


Fig. 29. Floor deformation implementation.

F_{platef}	$\begin{cases} R_c t_p + 2M_0 \left(\frac{\pi}{2} - \phi \right), & \text{if } N_0 u_0 < R_c t_p \\ N_0 u_0 + 2M_0 \left(\frac{\pi}{2} - \phi \right), & \text{if } N_0 u_0 \geq R_c t_p \end{cases}$
	$u_0 = s_{lf} \sqrt{(1 - \sin \phi)^2 \sin^2 \theta_p + (1 - \cos \theta_p)^2 \cos^2 \phi}$
F_{Bulk_i}	$\begin{cases} 0, & s_l \geq s_{lf} \\ \frac{\sigma_0 t_l \delta_{out} \left(1 - \frac{s_l}{B_{de}} \right)}{\sqrt{3}} \sqrt{\frac{1}{4} (\delta_{out} / B_{de})^2 \sin^2 \theta_p + (1 - \cos \theta_p)^2}, & 0 < s_l < s_{lf} \end{cases}$
F_{Bulk_f}	$\begin{cases} 0, & s_l \geq B_{de} \\ \frac{\sigma_0 t_l (B_{de} - s_l)}{\sqrt{3}} \sqrt{(1 - \sin \phi)^2 \sin^2 \theta_p + (1 - \cos \theta_p)^2 \cos^2 \phi}, & s_l < B_{de} \end{cases}$

$$\begin{aligned}
F_{Stif_i} &= \frac{4\sigma_0\delta_{out}\left(1 - \frac{s_l}{B_{de}}\right)(t_f d_f^2 + D_w t_w^2)}{\delta_{out}^2\left(1 - \frac{s_l}{B_{de}}\right)^2 + \chi_t^2} \\
F_{Stif_f} &= \frac{8\sigma_0(B_{de} - s_l)(t_f d_f^2 + D_w t_w^2)\tan\left(\frac{\pi}{4} - \frac{\phi}{2}\right)}{4(B_{de} - s_l)^2 \tan^2\left(\frac{\pi}{4} - \frac{\phi}{2}\right) + \chi_t^2} \\
F_{Gir} &= \begin{cases} \sigma_0 t_l (u_{0,l,out} - u_{0,l,in}) / \sqrt{3} & \\ u_{0,l,out} = \begin{cases} 0, & s_l \geq B_{de,out} \\ \delta_{out}\left(1 - \frac{s_l}{B_{de,out}}\right)\sqrt{\frac{1}{4}\left(\frac{\delta_{out}}{B_{de,out}}\right)^2 \sin^2 \theta_p + (1 - \cos \theta_p)^2}, & s_l < B_{de,out} \text{ and } \delta_{out} < \delta_{fra,out} \\ (B_{de,out} - s_l)\sqrt{(1 - \sin \phi)^2 \sin^2 \theta_p + (1 - \cos \theta_p)^2 \cos^2 \phi}, & s_l < B_{de,out} \text{ and } \delta_{out} \geq \delta_{fra,out} \end{cases} \\ u_{0,l,in} = \begin{cases} 0, & s_l \geq B_{de,inn} \\ \delta_{inn}\left(1 - \frac{s_{l,inn}}{B_{de,inn}}\right)\sqrt{\frac{1}{4}\left(\frac{\delta_{inn}}{B_{de,inn}}\right)^2 \sin^2 \theta_{p,inn} + (1 - \cos \theta_{p,inn})^2}, & s_l < B_{de,inn} \text{ and } \delta_{inn} < \delta_{fra,inn} \\ (B_{de,inn} - s_{l,inn})\sqrt{(1 - \sin \phi)^2 \sin^2 \theta_{p,inn} + (1 - \cos \theta_{p,inn})^2 \cos^2 \phi}, & s_l < B_{de,inn} \text{ and } \delta_{inn} \geq \delta_{fra,inn} \end{cases} \end{cases} \\
F_{floor} &= \frac{\sigma_0 t_l \Delta_t}{\tan \phi} \frac{b_{l,Gir} B_{de} + (\Delta_t - B_{de})\sqrt{b_{l,Gir}^2 + (\Delta_t - B_{de})^2 - B_{de}^2}}{b_{l,Gir}^2 + (\Delta_t - B_{de})^2} \\
&\quad + \frac{1}{2}\sigma_0 t_l^2 L_h^2 \left\{ \frac{b_{l,Gir}}{b_{l,Gir}^2 + (\Delta_t - B_{de})^2} - \frac{B_{de}}{\sqrt{(b_{l,Gir}^2 + (\Delta_t - B_{de})^2 - B_{de}^2)(b_{l,Gir}^2 + (\Delta_t - B_{de})^2)}} \right\}
\end{aligned}$$

Appendix D

The transformation of ship velocities from simplified FSI model coordinate system to LS-DYNA coordinate is implemented according to the equation:

$$\begin{aligned}
u_{CoG} &= u_{global} + q_{global}(T - K_G) \\
v_{CoG} &= v_{global} - p_{global}(T - K_G) + r_{global}X_G \\
w_{CoG} &= w_{global} - q_{global}X_G \\
p_{CoG} &= p_{global} \\
q_{CoG} &= -q_{global} \\
r_{CoG} &= -r_{global}
\end{aligned} \tag{31}$$

Appendix E. Input for the evaluation of plate split angle using LS DYNA

See Fig. 30.

Description	Symbol	Bare-Plate	Box-ship structure	Units
Grounding velocity	V	11	11	m/s
Ship length	L	100	100	m
Beam	B	16	16	m
Height of the rock from baseline		Varies	Varies	m
Rock tip radius	R_R	0.0	0.0	m
Semi-apex angle of cone (Rock)	ϕ	Varies	Varies	°
Spacing between longitudinal stiffeners	b_L	0.0	1.0	m
Spacing between inner and outer bottom	D_{DB}	0.0	2.0	m
Width of flange	d_f	0.0	0.0	m

Description	Symbol	Bare-Plate	Box-ship structure	Units
Height of longitudinal stiffener (height of web)	D_w	0.0	0.4	m
Height of transverse frame	D_t	0	2.0	m
Young's Modulus	E	2.058E+11	2.058E+11	Pa
Material strain hardening. Often ϵ_{cr}	n	0.1	0.1	-
Ductile fracture toughness of material	R_c	2.40E+05	2.40E+05	Pa·m
Thickness of flange	t_f	0.00	0.0	m
Web plate thickness (thickness of longitudinal girders)	t_l	0.0	0.015	m
Plate thickness	t	0.015	0.015	m
Thickness of transverse members (bulkheads, floors or frames)	t_t	0.0	0.015	m
Thickness of longitudinal web (stiffener)	t_w	0.0	0.0	m
Coulomb coefficient of friction	μ	0.3	0.3	-
Yield strength of material	σ_y	2.35E+08	2.35E+08	Pa
Flow stress of material	σ_0	2.35E+08	2.35E+08	Pa
Longitudinal spacing of transverse member	χt	0	2.0	m
Number of longitudinal girders		0	0	-

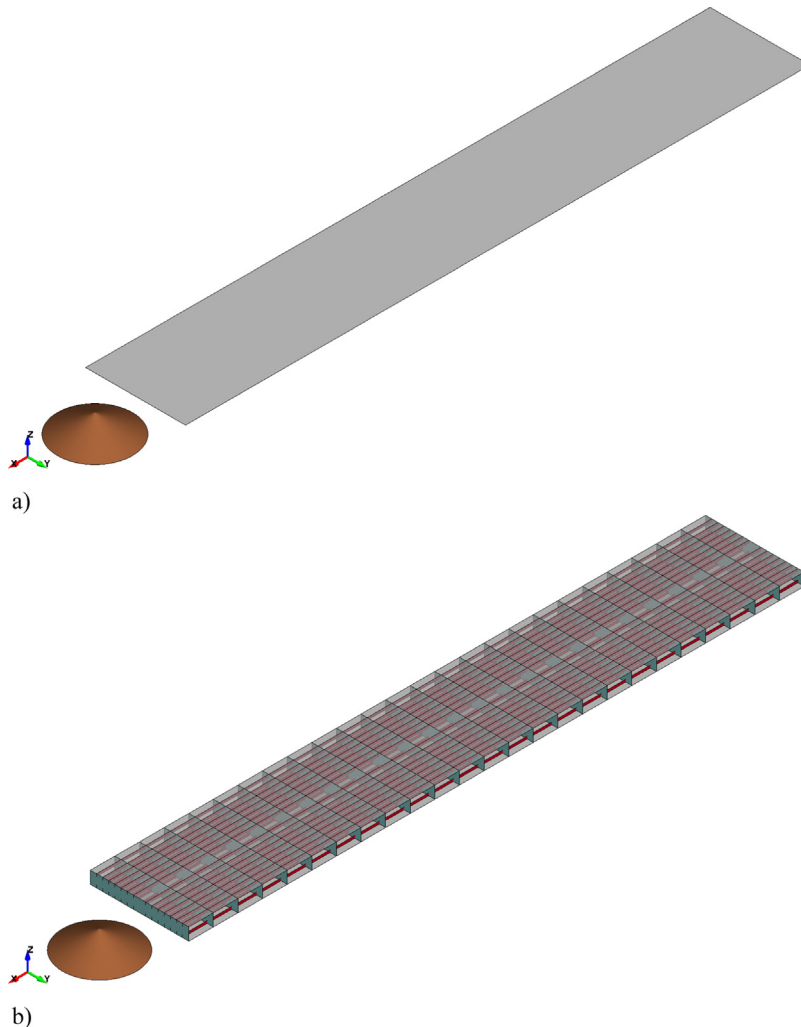


Fig. 30. (a) Bare-plate used for the evaluation of plate split angle at varying input conditions, (b) Fully structured box-ship used for the evaluation of plate split angle at varying input conditions.

Appendix F. Input for the evaluation of ship motions using LS-DYNA – MCOL

The hydrostatic restoring matrix \mathbf{K} , is calculated from Eq. (19) Appendix A. The added mass matrix \mathbf{M}_A and added damping matrix is obtained from strip theory (Journée, 1992). The added mass considered infinite frequency, whereas added damping comprise of 60 wave frequencies.

(i) Box ship input details

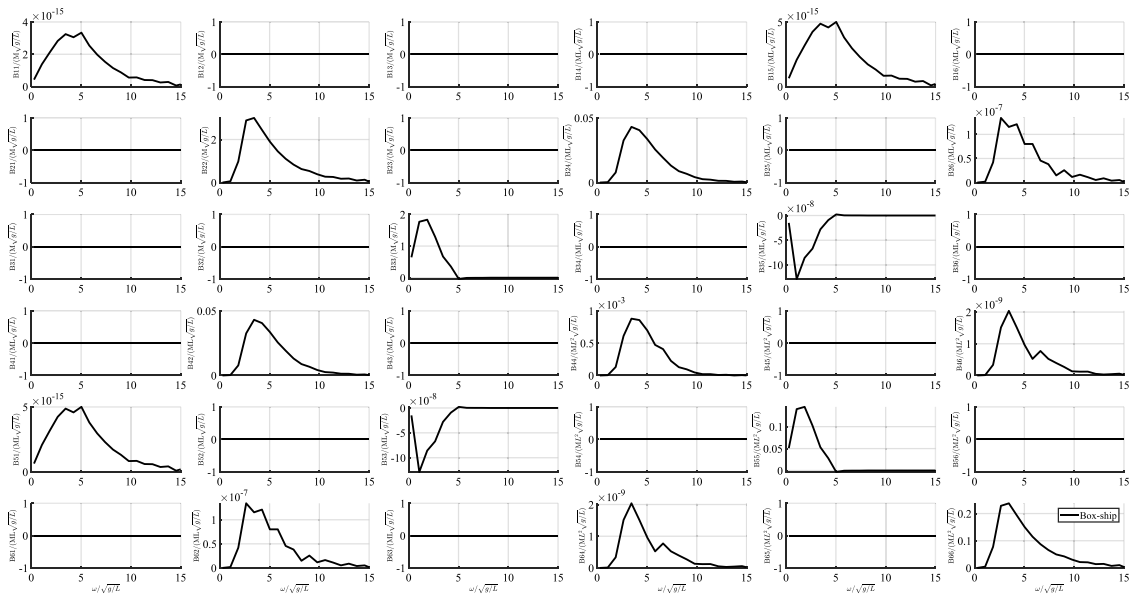
a. Restoring Matrix (units kg, m and s)

$$\mathbf{K} = \begin{bmatrix} 0 & 0 & 0 & 0 & 0 \\ 0 & 0 & 0 & 0 & 0 \\ 0 & 1.5691E + 07 & 0 & 0 & 0 \\ 0 & 0 & 3.3482E + 08 & 0 & 0 \\ 0 & 0 & 0 & 1.3071E + 10 & 0 \\ 0 & 0 & 0 & 0 & 0 \end{bmatrix}$$

b. Added mass matrix (units kg, m and s)

$$\mathbf{M}_A = - \begin{bmatrix} 1.4394E - 08 & 0 & 0 & 0 & 2.1591E - 08 & 0 \\ 0 & 3.6244E + 06 & 0 & 7.4031E + 06 & 0 & 8.3438E + 00 \\ 0 & 0 & 1.6271E + 07 & 0 & 8.5524E + 01 & 0 \\ 0 & 7.4031E + 06 & 0 & 1.5186E + 08 & 0 & 2.9333E + 01 \\ 2.1591E - 08 & 0 & 8.5524E + 01 & 0 & 1.2873E + 10 & 0 \\ 0 & 8.3438E + 00 & 0 & 2.9333E + 01 & 0 & 2.8676E + 09 \end{bmatrix}$$

c. Added damping (non-dimensional units) 60-wave frequencies



(ii) Passenger ship input details

a. Restoring Matrix (units kg, m and sec)

$$\mathbf{K} = \begin{bmatrix} 0 & 0 & 0 & 0 & 0 \\ 0 & 0 & 0 & 0 & 0 \\ 0 & 5.8359E + 07 & 0 & 1.5728E + 08 & 0 \\ 0 & 0 & 4.6316E + 09 & 0 & 0 \\ 0 & 1.5728E + 08 & 0 & 1.8073E + 11 & 0 \\ 0 & 0 & 0 & 0 & 0 \end{bmatrix}$$

b. Added mass matrix (units kg, m and sec)

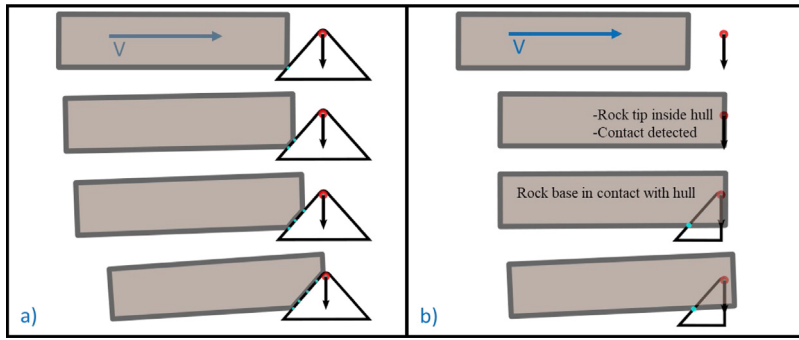
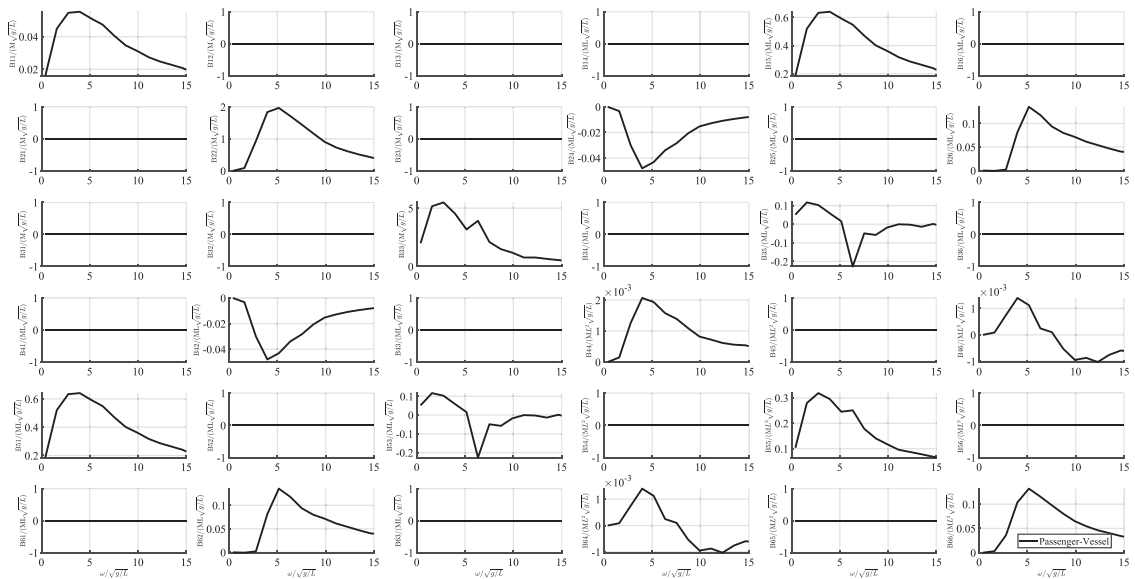


Fig. 31. (a) Illustration of LS-DYNA deformation, (b) Illustration of a simplified contact detection model, showing that after the initial contact the base of the rock is in contact with the ship. After the first contact, the deformation mode follows the method provided in Section 3.3 and Appendix B, C.

$$M_A = - \begin{bmatrix} 4.9025E + 05 & 0 & 0 & 0 & 5.6795E + 06 & 0 \\ 0 & 7.2461E + 06 & 0 & 5.9001E + 07 & 0 & 1.3638E + 08 \\ 0 & 0 & 7.8159E + 07 & 0 & 6.1460E + 08 & 0 \\ 5.6795E + 06 & 5.9001E + 07 & 0 & 1.4948E + 09 & 0 & 3.8823E + 08 \\ 0 & 1.3638E + 08 & 0 & 3.8823E + 08 & 1.6907E + 11 & 0 \\ 0 & 0 & 0 & 0 & 0 & 2.5242E + 10 \end{bmatrix}$$

c. Added damping (non-dimensional units) 60-wave frequencies



Appendix G

A comparison of the simplified contact model against LS-DYNA simulations is illustrated in Fig. 31. LS-DYNA considers the complete contact in between the surface of the hull and rock. This is illustrated in Fig. 31(a), where the hull bottom touches the generator of the cone at some distance from the tip of the rock. In the simplified FSI model the contact is detected once the tip is inside the hull (i.e., penetration into the hull becomes δ_{out}). After the first contact, the deformation mode follows the pattern described in Section 3.3 and Appendices B and C.

Appendix H. Supplementary data

Supplementary material related to this article can be found online at <https://doi.org/10.1016/j.jfluidstructs.2022.103589>.

References

- Abubakar, A., Dow, R.S., 2013. Simulation of ship grounding damage using the finite element method. *Int. J. Solids Struct.* 50, 623–636. <http://dx.doi.org/10.1016/j.ijsolstr.2012.10.016>.
- Allianz Global, 2020. Safety and shipping review 2020. In: *An Annual Review of Trends and Developments in Shipping Losses and Safety*. Allianz Global Corporate & Specialty.
- Alsos, H.S., Amdahl, J., 2007. On the resistance of tanker bottom structures during stranding. *Mar. Struct.* 20, 218–237. <http://dx.doi.org/10.1016/j.marstruct.2007.06.001>.
- Badouel, D., 1990. An efficient ray - polygon intersection. In: *Graphics Gems*. Elsevier Inc., pp. 390–393. <http://dx.doi.org/10.1016/B978-0-08-050753-8.50082-6>.
- Brix, J.E., 1993. *Manoeuvring Technical Manual*. Seehafen Verlag, Hamburg, Germany.
- Brubak, L., Hu, Z., Kõrgesaar, M., Schipperen, I., Tabri, K., 2021. Numerical simulations of grounding scenarios – benchmark study on key parameters in FEM modelling. In: *Lecture Notes in Civil Engineering*. pp. 257–269. http://dx.doi.org/10.1007/978-981-15-4672-3_16.
- Buldgen, L., Le Sourne, H., Besnard, N., Rigo, P., 2012. Extension of the super-elements method to the analysis of oblique collision between two ships. *Mar. Struct.* <http://dx.doi.org/10.1016/j.marstruct.2012.08.002>.
- Calle, M.A.G., Oshiro, R.E., Alves, M., 2017. Ship collision and grounding: Scaled experiments and numerical analysis. *Int. J. Impact Eng.* 103, 195–210. <http://dx.doi.org/10.1016/j.ijimpeng.2017.01.021>.
- Calle, M.A.G., Salmi, M., Mazzariol, L.M., Kujala, P., 2020. Miniature reproduction of raking tests on marine structure: Similarity technique and experiment. *Eng. Struct.* 212, 110527. <http://dx.doi.org/10.1016/j.engstruct.2020.110527>.
- Chen, B.Q., Guedes Soares, C., 2020. Numerical investigation on the influence of stiffeners on the crushing resistance of web girders in ship grounding. In: *Developments in the Collision and Grounding of Ships and Offshore Structures - Proceedings of the 8th International Conference on Collision and Grounding of Ships and Offshore Structures, ICCGS 2019*. CRC Press/Balkema, pp. 49–56. <http://dx.doi.org/10.1016/j.marstruct.2018.10.003>.
- Choung, J., Lee, K., Park, B., 2020. Advanced numerical technique of ship collision considering fluid effect. In: *Developments in the Collision and Grounding of Ships and Offshore Structures - Proceedings of the 8th International Conference on Collision and Grounding of Ships and Offshore Structures, ICCGS 2019*. CRC Press/Balkema, pp. 105–110. <http://dx.doi.org/10.1201/9781003002420-13>.
- Clarke, D., Gedling, P., Hine, G., 1982. *The Application of Manoeuvring Criteria in Hull Design using Linear Theory*. Transactions of the Royal Institution of Naval Architects.
- Conti, F., Le Sourne, H., Vassalos, D., Kujala, P., Lindroth, D., Kim, S.J., Hirdaris, S., 2021. A comparative method for scaling SOLAS collision damage distributions based on ship crashworthiness—application to probabilistic damage stability analysis of a passenger ship. *Ships Offshore Struct.* <http://dx.doi.org/10.1080/17445302.2021.1932023>.
- Descantes, Y., Tricoire, F., Richard, P., 2019. Classical contact detection algorithms for 3D DEM simulations: Drawbacks and solutions. *Comput. Geotech.* 114, <http://dx.doi.org/10.1016/j.compgeo.2019.103134>.
- Ehlers, S., 2011. A review of collision and grounding damage assessment methods. *Mar. Syst. Ocean Technol.* 6, 5–15. <http://dx.doi.org/10.1007/bf03449252>.
- Faltinsen, O.M., 1990. *Sea Loads on Ships and Offshore Structures*. Cambridge University Press.
- Faltinsen, O.M., Minsaas, K.J., Liapis, N., Skjoldal, S.O., 1980. Prediction of resistance and propulsion of a ship in a seaway. In: *Proceedings of the 13th Symposium on Naval Hydrodynamics*, Tokyo. pp. 1–19.
- Ferry, M., Le Sourne, H., Besnier, F., 2002. *MCOL-theoretical manual*. Principia Mar. Nantes.
- Fossen, T.I., 2011. *HandBook of Marine Craft Hydrodynamics and Motion Control*, HandBook of Marine Craft Hydrodynamics and Motion Control. John Wiley and Sons, <http://dx.doi.org/10.1002/9781119994138>.
- Frank, W., 1967. Oscillation of cylinders in or below the free surface of deep fluids. *David W. Taylor Nav. Sh. Res. Dev. Center*.
- Gil, M., Montewka, J., Krata, P., Hinz, T., Hirdaris, S., 2020. Determination of the dynamic critical maneuvering area in an encounter between two vessels: Operation with negligible environmental disruption. *Ocean Eng.* 213, 107709. <http://dx.doi.org/10.1016/j.oceaneng.2020.107709>.
- Heinvee, M., Tabri, K., 2015. A simplified method to predict grounding damage of double bottom tankers. *Mar. Struct.* 43, 22–43. <http://dx.doi.org/10.1016/j.marstruct.2015.04.002>.
- HELCOM – Helsinki Commission, 2021. Ship accidents in the Baltic sea during the period 1989 to 2018. Retrieved from [WWW Document]. URL <https://metadata.helcom.fi/geonetwork/srv/eng/catalog/search#/metadata/cae61cf8-0b3a-449a-aeaf-1df752dd3d80>. (Accessed 5 November 2021).
- Hirdaris, S.E., Bai, W., Dessi, D., Ergin, A., Gu, X., Hermundstad, O.A., Huijismans, R., Iijima, K., Nielsen, U.D., Parunov, J., Fonseca, N., Papanikolaou, A., Argyriadis, K., Incecik, A., 2014. Loads for use in the design of ships and offshore structures. *Ocean Eng.* 78, 131–174. <http://dx.doi.org/10.1016/j.oceaneng.2013.09.012>.
- Hirdaris, Spyros, Mikkola, Tommi, 2021. In: *Hirdaris, Spyros, Mikkola, Tommi (Eds.), Ship Dynamics for Performance Based Design and Risk Averse Operations*, 1st ed. 1. MDPI, Basel, Switzerland ISBN: 978-3-0365-0617-3, pp. 1–253.
- Hong, L., Amdahl, J., 2012. Rapid assessment of ship grounding over large contact surfaces. *Ships Offshore Struct.* 7, 5–19. <http://dx.doi.org/10.1080/17445302.2011.579003>.
- Idrisova, S., Bergström, M., Hirdaris, S.E., Kujala, P., 2019. Analysis of a collision-energy-based method for the prediction of ice loading on ships. *Appl. Sci.* 9, <http://dx.doi.org/10.3390/app9214546>.
- Jones, N., 2011. *Structural Impact*. Cambridge University Press, Cambridge. <http://dx.doi.org/10.1017/CBO9780511820625>.
- Journée, J.M., 1992. Quick strip theory calculations in ship design. In: *PRADS'92 Conf. Pract. Des. Ships Mob. Units*, vol. 1.
- Kim, S.J., Kõrgesaar, M., Ahmadi, N., Taimuri, G., Kujala, P., Hirdaris, S., 2021. The influence of fluid structure interaction modelling on the dynamic response of ships subject to collision and grounding. *Mar. Struct.* 75, <http://dx.doi.org/10.1016/j.marstruct.2020.102875>.
- Kim, S.J., Kõrgesaar, M., Taimuri, G., Kujala, P., Hirdaris, S., 2020. A quasi-dynamic approach for the evaluation of structural response in ship collisions and groundings. In: *Proceedings of the International Offshore and Polar Engineering Conference*. International Society of Offshore and Polar Engineers, pp. 3174–3180.
- Kim, S.J., Sohn, J.M., Kujala, P., Hirdaris, S., 2022a. A simplified fluid structure interaction model for the assessment of ship hard grounding. *J. Mar. Sci. Technol.* 27, 695–711. <http://dx.doi.org/10.1007/s00773-021-00862-6>.
- Kim, S.J., Taimuri, G., Kujala, P., Conti, F., Le Sourne, H., Pineau, J.P., Looten, T., Bae, H., Mujeeb-Ahmed, M.P., Vassalos, D., Kaydihan, L., Hirdaris, S., 2022b. Comparison of numerical approaches for structural response analysis of passenger ships in collisions and groundings. *Mar. Struct.* 81, 103125. <http://dx.doi.org/10.1016/j.marstruct.2021.103125>.
- Kitamura, O., Kuriowa, T., 1996. Large-scale grounding experiments and numerical simulations. *Ship Technol. Res.* 43, 62–69.
- Lakshminarayanan, P.A.K., Hirdaris, S., 2020. Comparison of nonlinear one- and two-way FFSI methods for the prediction of the symmetric response of a containership in waves. *Ocean Eng.* 203, 107179. <http://dx.doi.org/10.1016/j.oceaneng.2020.107179>.
- Le Sourne, H., 2007. A ship collision analysis program based on super-element method coupled with large rotational ship movement analysis tool. In: *International Conference on Collision and Grounding of Ships*. pp. 131–138.

- Le Sourne, H., Besnard, N., Cheylan, C., Buannic, N., 2012. A ship collision analysis program based on upper bound solutions and coupled with a large rotational ship movement analysis tool. *J. Appl. Math.* 2012, 375686. <http://dx.doi.org/10.1155/2012/375686>.
- Lee, S.G., Lee, J.S., Lee, H.S., Park, J.H., Jung, T.Y., 2017. Full-scale ship collision, grounding and sinking simulation using highly advanced M & S system of FSI analysis technique. In: *Procedia Engineering*. Elsevier Ltd, pp. 1507–1514. <http://dx.doi.org/10.1016/j.proeng.2016.12.232>.
- Lee, S.G., Zhao, T., Nam, J.H., 2013. Structural safety assessment of ship collision and grounding using FSI analysis technique. In: *Collision and Grounding of Ships and Offshore Structures - Proceedings of the 6th International Conference on Collision and Grounding of Ships and Offshore Structures, ICCGS 2013*. Taylor and Francis - Balkema, pp. 197–204. <http://dx.doi.org/10.1201/b14915-24>.
- Lehmann, E., Egge, E.D., Scharrer, M., Zhang, L., 2001. Calculation of collisions with the aid of linear fe models. In: *Practical Design of Ships and Other Floating Structures. Proceedings of the Eighth International Symposium on Practical Design of Ships and Other Floating Structures PRADS, Practical Design in Shipbuilding Chinese Academy of Engineering*. Chinese Society O, pp. 1293–1300.
- Lemmen, P.M., Vredeveltd, W., Pinkster, J.A., 1996. Design analysis for grounding experiments. In: *International Conference on Designs and Grounding Protection of Ships*, San Francisco, California, August 22-23. pp. 6.
- Lewandowski, E.M., 2004. *The dynamics of marine craft maneuvering and seakeeping*. In: *Advanced Series on Ocean Engineering*, vol. 22.
- Liu, B., Villavicencio, R., Pedersen, P.T., Guedes Soares, C., 2021. Analysis of structural crashworthiness of double-hull ships in collision and grounding. *Mar. Struct.* <http://dx.doi.org/10.1016/j.marstruc.2020.102898>.
- Liu, B., Villavicencio, R., Zhang, S., Guedes Soares, C., 2017. Assessment of external dynamics and internal mechanics in ship collisions. *Ocean Eng.* 141, 326–336. <http://dx.doi.org/10.1016/j.oceaneng.2017.06.053>.
- Longuet-Higgins, M.S., 1977. The mean forces exerted by waves on floating or submerged bodies with applications to sand bars and wave power machines. *Proc. R. Soc. A* 352, 463–480. <http://dx.doi.org/10.1098/rspa.1977.0011>.
- LSTC, 2021. *LS-DYNA: Keyword user's manual, ls-dyna R12.0*. California, USA.
- Lu, T., Zou, Z., 2020. Numerical study of brash ice loads on ship hulls based on DEM-CFD. In: *Proceedings of the 6th European Conference on Computational Mechanics: Solids, Structures and Coupled Problems, ECCM 2018 and 7th European Conference on Computational Fluid Dynamics, ECFD 2018*. pp. 4390–4402.
- Luhman, Henning, Routi, Anna-Lea, Cardinale, Mike, Rodolphe, Bertin, Gijs, Streppel, Juha, Kujanpää, 2019. Deliverable 2.1, Sample Ships - Overview, EU Horizons 2020 project on Flooding Accident Response (FLARE), Grant agreement No. 814753. FLARE Consortium, EU, https://www.flare-project.eu/images/D2.1_overview_sample_ships_final_20210215.pdf.
- Luhmann, H., 2009. *Integrated flooding and standard for stability and crises management*. FLOODSTAND deliverable No. D1.1b. Report FP7-RTD-218532.
- Luo, W., Jiang, D., Wu, T., Guo, C., Wang, C., Deng, R., Dai, S., 2020. Numerical simulation of an ice-strengthened bulk carrier in brash ice channel. *Ocean Eng.* 196, 106830. <http://dx.doi.org/10.1016/j.oceaneng.2019.106830>.
- Manderbacka, T., Mikkola, T., Ruponen, P., Matusiak, J., 2015. Transient response of a ship to an abrupt flooding accounting for the momentum flux. *J. Fluids Struct.* 57, 108–126. <http://dx.doi.org/10.1016/j.jfluidstructs.2015.06.001>.
- Matusiak, J., 2002. Transient motion of ship during hard grounding. In: *Proceedings of the 6th International Ship Stability Workshop*, Webb Institute, Proceedings. Paper: P2002-1 Proceedings.
- Matusiak, J.E., 2021. Dynamics of a rigid ship - with applications, Aalto university, Aalto university publication series SCIENCE + TECHNOLOGY; 4/2021., Aalto university. <http://urn.fi/URN:ISBN:978-952-64-0399-1>.
- Minorsky, V.U., 1958. *An Analysis of Ship Collisions with Reference to Protection of Nuclear Power Plants*.
- Moller, T., Trumbore, B., 1998. Fast, minimum storage ray-triangle intersection. In: *Doktorsavhandlingar Vid Chalmers Tekniska Hogskola*. Chalmers Tekniska Hogskola, <http://dx.doi.org/10.1201/b10628-23>.
- Nguyen, T.H., Amdahl, J., Garrè, L., Leira, B.J., 2011. A study on dynamic grounding of ships. In: *Advances in Marine Structures - Proceedings of the 3rd International Conference on Marine Structures, MARSTRUCT 2011*. pp. 373–380. <http://dx.doi.org/10.1201/b10771-46>.
- Paik, J.K., Kim, K.J., Lee, J.H., Jung, B.G., Kim, S.J., 2017. Test database of the mechanical properties of mild, high-tensile and stainless steel and aluminium alloy associated with cold temperatures and strain rates. *Ships Offshore Struct.* 12, S230–S256. <http://dx.doi.org/10.1080/17445302.2016.1262729>.
- Pill, I., Tabri, K., 2011. Finite element simulations of ship collisions: A coupled approach to external dynamics and inner mechanics. *Ships Offshore Struct.* 6, 59–66. <http://dx.doi.org/10.1080/17445302.2010.509585>.
- Prabowo, A.R., Cao, B., Sohn, J.M., Bae, D.M., 2020. Crashworthiness assessment of thin-walled double bottom tanker: Influences of seabed to structural damage and damage-energy formulae for grounding damage calculations. *J. Ocean Eng. Sci.* 5, 387–400. <http://dx.doi.org/10.1016/j.joes.2020.03.002>.
- Prabowo, A.R., Cho, H.J., Lee, S.G., Bae, D.M., Sohn, J.M., Cho, J.H., 2017. Investigation on the structural damage of a double-hull ship, part II - grounding impact. In: *Procedia Structural Integrity*. Elsevier B.V., pp. 943–950. <http://dx.doi.org/10.1016/j.prostr.2017.07.129>.
- Rizzuto, E., Brubak, L., Kim, G.S., Kõrgesaar, M., Nahshon, K., Nilva, A., Schipperen, I., Stadie-Frohboes, G., Suzuki, K., Tabri, K., Wægter, J., 2018. Committee V.1: Accidental limit states. In: *Proceedings of the 20th International Ship and Offshore Structures Congress, ISSC 2018 - Specialist Committee Reports*.
- Rodd, J.L., 1996a. Large scale tanker grounding experiments. In: *Proceedings of the International Offshore and Polar Engineering Conference*. pp. 483–494.
- Rodd, J.L., 1996b. Observations on conventional and advanced double hull grounding experiments. In: *Int. Conf. on Designs and Methodologies for Collision and Grounding Protection of Ships*. pp. 11–13.
- Rodd, J.L., Sikora, J.P., 1995. Double hull grounding experiments. In: *Proceedings of the International Offshore and Polar Engineering Conference*. pp. 446–456.
- Rudan, S., Čatipović, I., Berg, R., Völkner, S., Prebeg, P., 2019. Numerical study on the consequences of different ship collision modelling techniques. *Ships Offshore Struct.* 14, 387–400. <http://dx.doi.org/10.1080/17445302.2019.1615703>.
- Sakamoto, T., Baba, E., 1986. Minimization of resistance of slowly moving full hull forms in short waves. In: *Proceedings of Sixteenth Symposium on Naval Hydrodynamics*. pp. 598–613.
- Simonsen, B.C., 1997a. *Mechanics of ship grounding*.
- Simonsen, B.C., 1997b. Ship grounding on rock - II. Validation and application. *Mar. Struct.* 10, 563–584. [http://dx.doi.org/10.1016/S0951-8339\(98\)00003-3](http://dx.doi.org/10.1016/S0951-8339(98)00003-3).
- Simonsen, B.C., 1997c. Ship grounding on rock - I. Theory. *Mar. Struct.* 10, 519–562. [http://dx.doi.org/10.1016/S0951-8339\(98\)00002-1](http://dx.doi.org/10.1016/S0951-8339(98)00002-1).
- Song, Z., Hu, Z., 2017. An integrated analytical tool on predicting structural responses of ships under collision and grounding scenarios. In: *Proceedings of the International Conference on Offshore Mechanics and Arctic Engineering - OMAE*, 57656. <http://dx.doi.org/10.1115/OMAE201761220>.
- Song, M., Kim, E., Amdahl, J., Ma, J., Huang, Y., 2016. A comparative analysis of the fluid–structure interaction method and the constant added mass method for ice-structure collisions. *Mar. Struct.* 49, 58–75. <http://dx.doi.org/10.1016/j.marstruc.2016.05.005>.
- Song, M., Ma, J., Huang, Y., 2017. Fluid–structure interaction analysis of ship-ship collisions. *Mar. Struct.* 55, 121–136. <http://dx.doi.org/10.1016/j.marstruc.2017.05.006>.
- Souliotis, C., Samuelides, M.S., 2013. Loading on stranded ships. In: *Collision and Grounding of Ships and Offshore Structures - Proceedings of the 6th International Conference on Collision and Grounding of Ships and Offshore Structures, ICCGS 2013*. pp. 143–149. <http://dx.doi.org/10.1201/b14915-18>.

- Sun, B., Hu, Z., Wang, J., 2017. Bottom structural response prediction for ship-powered grounding over rock-type seabed obstructions. *Mar. Struct.* 54, 127–143. <http://dx.doi.org/10.1016/j.marstruc.2017.04.002>.
- Taimuri, G., Matusiak, J., Mikkola, T., Kujala, P., Hirdaris, S., 2020. A 6-DoF maneuvering model for the rapid estimation of hydrodynamic actions in deep and shallow waters. *Ocean Eng.* 218, 108103. <http://dx.doi.org/10.1016/j.oceaneng.2020.108103>.
- Taimuri, G., Mikkola, T., Matusiak, J., Kujala, P., Hirdaris, S., 2019. The influence of hydrodynamic assumptions on ship maneuvering. In: 22nd Numerical Towing Tank Symposium, NuTTS 2019-Tomar, Portugal. pp. 6.
- Vantorre, M., 2001. Manoeuvring coefficients for a container carrier in shallow water: An evaluation of semi-empirical formulae. In: Mini Symposium on Prediction of Ship Manoeuvring Performance, 18, 2001, Tokyo, Japan.
- Vantorre, M., Eloit, K., Delefortrie, G., Lataire, E., Candries, M., Verwilligen, J., 2017. Maneuvering in shallow and confined water. In: *Encyclopedia of Maritime and Offshore Engineering*. John Wiley & Sons, Ltd, pp. 1–17.
- Wang, J., Derradji-Aouat, A., 2010. Ship Performance in Broken Ice Floes-Preliminary Numerical Simulations. Report No. TR-2010-24, Institute for Ocean Technology, National Research Council, St. John's, NL, Canada.
- Yu, Z., Amdahl, J., 2016. Full six degrees of freedom coupled dynamic simulation of ship collision and grounding accidents. *Mar. Struct.* 47, 1–22.
- Yu, Z., Liu, Z., Amdahl, J., 2019. Discussion of assumptions behind the external dynamic models in ship collisions and groundings. *Ships Offshore Struct.* 14, 45–62. <http://dx.doi.org/10.1080/17445302.2018.1556234>.
- Yu, Z., Shen, Y., Amdahl, J., Greco, M., 2016. Implementation of linear potential-flow theory in the 6DOF coupled simulation of ship collision and grounding accidents. *J. Ship Res.* 60, 119–144. <http://dx.doi.org/10.5957/JOSR.60.3.160012>.
- Zeng, J., Hu, Z., Chen, G., 2016. A steady-state plate tearing model for ship grounding over a cone-shaped rock. *Ships Offshore Struct.* <http://dx.doi.org/10.1080/17445302.2014.985429>.
- Zhang, M., Kujala, P., Hirdaris, S., 2022. A machine learning method for the evaluation of ship grounding risk in real operational conditions. *Reliab. Eng. Syst. Saf.* (submitted for publication).
- Zhang, M., Montewka, J., Manderbacka, T., Kujala, P., Hirdaris, S., 2021. A big data analytics method for the evaluation of ship-ship collision risk reflecting hydrometeorological conditions. *Reliab. Eng. Syst. Saf.* 213, 107674. <http://dx.doi.org/10.1016/j.res.2021.107674>.
- Zhang, S., Pedersen, P.T., Villavicencio, R., 2019. Internal mechanics of ship collision and grounding. In: Butterworth-Heinemann (Ed.), *Probability and Mechanics of Ship Collision and Grounding*, 1st ed. Elsevier, ISBN: 978-0-12-815022-1, pp. 147–270.
- Zhang, A., Suzuki, K., 2006. Numerical simulation of fluid–structure interaction of liquid cargo filled tank during ship collision using the ALE finite element method. *Int. J. Crashworthiness* 11, 291–298. <http://dx.doi.org/10.1533/ijcr.2005.0105>.